Department of Physics and Astronomy

University of Heidelberg

Master thesis

in Physics

submitted by

Manuel Kramer

born in Leonberg

2019

Hydrodynamics of the Common Envelope Phase of sdB Stars

This Master thesis has been carried out by Manuel Kramer

at the

Heidelberg Institute for Theoretical Studies

under the supervision of

Prof. Dr. Friedrich Röpke

(Hydrodynamik der Phase der Gemeinsamen Hülle von sdB-Sternen):

Die Phase der Gemeinsamen Hülle ist ein entscheidender Schritt in der Entstehung enger Binärsystemen mit mindestens einem kompakten Begleiter. Diese Phase wird eingeleitet, wenn ein Stern das Entwicklungsstadium eines Roten Riesen erreicht und sich zu einem solchen Ausmaß ausdehnt, dass der Begleiter vollkommen umschlossen wird. Ein heißer B-Typ Unterzwerg (sdB) entsteht, wenn ein Stern an der Spitze des Roten Riesenasts seine gesamte Hülle während der Phase der Gemeinsamen Hülle verliert.
Diese Arbeit verwendet AREPO, einen Hydrodynamikcode auf einem bewegten Gitter, um die Phase der Gemeinsamen Hülle von sdB-Sternen mit leichten Begleitern zu simulieren. Ein Anfangsmodell wird erstellt, indem ein MESA Profil auf das Gitter von AREPO projeziert wird. Anschließend wird eine Relaxation durchgeführt, um ein stabiles Modell eines Sterns an der Spitze des Roten Riesenasts zu erhalten. Es werden spezielle Gitterverfeinerungen verwendet, um eine hohe Auflösung um den Kern des Riesens und seines Begleiters zu gewährleisten.
Die Simulationen zeigen, dass auch Begleiter mit sehr niedrigen Massen im Bereich von $0.05\,\mathrm{M}_\odot$ und $0.1\,\mathrm{M}_\odot$ ausreichen, um beinahe die gesamte Hülle auszustoßen. Dies stimmt mit jüngsten Beobachtungen überein und hebt die Bedeutung der Phase der Gemeinsamen Hülle für die Entwicklung von sdB-Sternen hervor.

(Hydrodynamics of the Common Envelope Phase of sdB-Stars):

The common envelope (CE) phase is essential for the formation of close binary systems with at least one compact companion. This phase is initiated when one star reaches the red giant branch (RGB) and expands to such an extend that the companion is completely engulfed. To form a hot subluminous B-type (sdB) star, a giant at the tip of the RGB has to lose all its envelope during the CE phase.
This work applies the moving-mesh hydrodynamics code AREPO to simulate the CE phase of sdB stars with low-mass companions. An initial model is generated by mapping a MESA profile onto the grid of AREPO, followed by a relaxation run to achieve a stable representation of a star at the tip of the RGB. Special refinement criteria are used to ensure high resolution around the cores of the red giant (RG) and the companion.
The simulations show that even very low mass companions in the range of $0.05\,\mathrm{M}_\odot$ to $0.1\,\mathrm{M}_\odot$ can cause an almost complete unbinding of the envelope. This is in agreement with recent observations and emphasizes the importance of common envelope evolution (CEE) for the formation of sdB stars.

Contents

1 Hot Subluminous B-type Stars 1
1.1 Physical Properties 1
1.2 Formation 1
1.3 Observations 3

2 Common Envelope Evolution 5
2.1 Introduction 5
2.2 Main Phases 5
2.3 Energy Budget and Alpha Formalism 7
2.4 Angular Momentum 7
2.5 Ionization Energy 8

3 Numerical Methods 11
3.1 AREPO 11
3.2 Finite Volume Hydrodynamics 11
3.3 Gravity in AREPO 13
3.4 Simplifications 14

4 Initial Models 15
4.1 Mesa Profiles 15
4.2 Relaxation 16
4.3 Simulation and Results 18

5 A First Common Envelope Simulation with a Light Companion 21
5.1 Setup 21
5.2 Results and Discussion 22
5.3 Conclusion 28

6 The Influence of Initial Parameters 29
6.1 Resolution Study 29
6.2 The Effect of Varying Companion Masses 31
6.3 Discussion 34

7 Conclusion 37
7.1 Achievements 37
7.2 Outlook 38

I Appendix 41

A Lists 43
1.1 List of Figures 43
1.2 List of Tables 44

B Bibliography 47

1 Hot Subluminous B-type Stars

This chapter aims to provide background information about sdB stars, as the simulations presented later in this work are focused on getting insights on their formation process. We first explain what physical properties are characteristic for sdB stars, followed by the formation process and some recent observational findings.

1.1 Physical Properties

The following section is based on the work from Heber (2016, 2009). Hot subluminous B-type stars are a late stage in the evolution of low-mass stars. They have masses of about $0.5\,\mathrm{M}_{\odot}$ and burn helium in their core. Despite their small size of around $0.15\,\mathrm{R}_{\odot}$ to $0.25\,\mathrm{R}_{\odot}$, they have very high surface temperatures of about 20 000 K to 40 000 K. Hence, they can be found on the blue end of the horizontal branch (HB) in the Hertzsprung-Russell (HR) diagram, that is also called extreme horizontal branch (EHB). The hydrogen envelopes of sdB stars are too thin to allow hydrogen shell burning, which distinguishes them from other HB stars. SdB stars are the remaining core of RG stars which have lost all of their envelope material. It has been shown that many sdB stars are part of a binary system of which a significant fraction has low mass companions (Geier et al., 2011; Schaffenroth et al., 2014). Since the radius of the RG progenitor often exceeds the orbital separation of the observed binary system, a previous undergoing of a CE phase is strongly implied (Maxted et al., 2001). While the companion orbits within the envelope of the RG, it transfers orbital angular momentum and energy to the gas of the envelope, which can ultimately lead to an ejection (Ivanova et al., 2013). Among the various systems that arise from CE evolution, the sdB systems represent an interesting case as they are non-interacting when for example compared to cataclysmic variables, thus the systems properties can be determined with higher precision. Companions of sdB stars comprise a wide range of different stellar objects from black hole (BH) and neutron star (NS) to main sequence (MS) and substellar companions with only a few Jupiter masses (Schaffenroth et al., 2014).

1.2 Formation

There are two main scenarios that are discussed as possible channels for sdB star formation. The first option is the merger of two helium white dwarfs (WDs) that result in a single sdB star. The second one starts with a binary system consisting of a RG star and a compact companion that undergo a CE phase. The high fraction

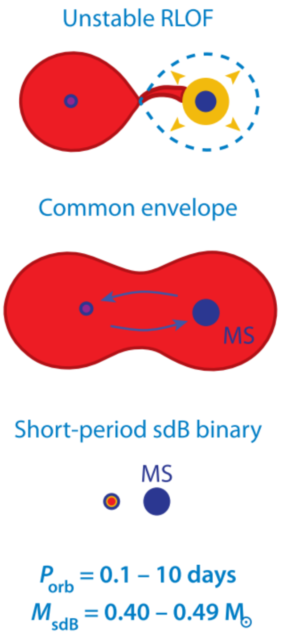
Unstable RLOF
Common envelope
MS
Short-period sdB binary
MS
P_{orb} = 0.1 – 10 days
M_{sdB} = 0.40 – 0.49 $M_{\odot}$

Figure 1.1: Formation channel for sdB stars through CEE with an MS companion. The core of the evolved RG is depicted in purple and the surrounding mass of the envelope in red. After the CE phase, the core of the RG remains as a sdB star in a close binary with the companion. The figure is modified from Podsiadlowski et al. (2008).

of sdB stars in close binary systems clearly shows the importance of CE interaction in the formation process (Heber, 2009, 2016). We will discuss the second formation channel in more detail, as our simulation will aim to emulate the CE formation process.

Formation via Common Envelope Evolution

In Figure (1.1), the schematic formation process is illustrated. The sdB progenitor has already evolved to the tip of the RG branch and hence expanded considerably. It fills out its Roche lobe (RL) and, supposing the binary companion is close enough, mass transfer is triggered. A so called Roche lobe overflow (RLOF) sets in and, in case of dynamically instable mass transfer, the two stars will form a CE. Even stable mass transfer can lead to a CE, if the companion is unable to accrete at a high enough rate or mass is not ejected rapidly enough (Ivanova et al., 2013; Heber, 2016). The companion traverses the material of the envelope and scatters gas particles into its wake. The emerging overdensity behind the companion exerts a gravitational drag force and makes it lose orbital energy and angular momentum, which is transferred to the gas particles of the envelope. If the energy transferred to the envelope is high enough, some parts can become unbound and ejection from the system ensues. At the same time, the companion will move further inward onto closer orbits and continue to transfer energy to the envelope, which can ultimately lead to a complete unbinding. In addition, there are more energy sources that contribute to the ejection of the envelope mass, such as helium and hydrogen recombination (Han et al., 1995), winds and convection.

Since the timescale of the spiral-in is on the order of a dynamical timescale and thus short when compared to the stellar lifetime, the more compact companion star

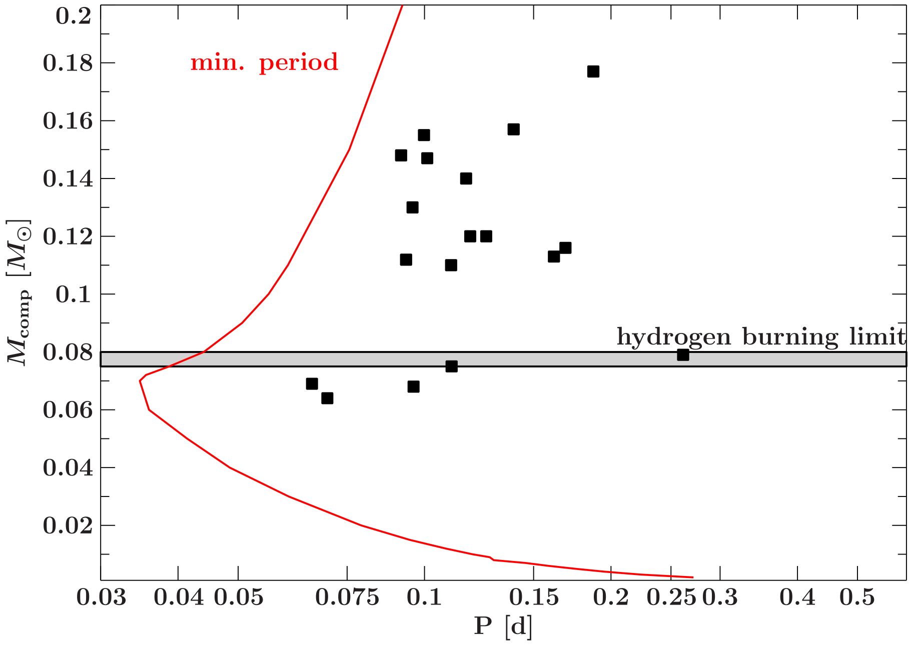

Figure 1.2: Diagram of the companion mass over period for known HR Vir systems. The hydrogen burning limit is indicated by the gray horizontal bar. All companions below are in the sub-stellar regime. The red line depicts the minimal possible period for a specific mass and is based on the assumption that the companions cannot exceed the Roche limit. The figure is take from Schaffenroth et al. (2017).

normally remains almost unchanged. After ejection of the envelope, the core of the RG star and the companion are left as a close binary with typical periods between 0.1 days to 10 days (Heber, 2016).

The stripped core of the RG star is helium burning, has very little to none hydrogen left in the atmosphere and therefore exhibits the physical characteristics of a sdB star. The small variance in mass for sdB stars can be explained by the fact that all low-mass stars with masses from $0.8\,\mathrm{M}_\odot$ to $2\,\mathrm{M}_\odot$ will develope a degenerate core while climbing the RGB, as they are not massive enough to quietly start helium core burning. They reach the tip of the RGB when the core mass was increased by shell burning to about half a solar mass. At this point, the gravitational pressure of the core is high enough to ignite helium burning which will lift the degeneracy of the core in a runaway process that is better known as the helium flash (Girardi, 2016). If the envelope is stripped in this phase of the stellar evolution of the RG primary by CE interaction, a sdB binary system is formed. Hence, it exists an interesting degeneracy for the final mass of sdB star, as it is not dependant on the initial mass of the RG progenitor.

1.3 Observations

Recent publications have observed potential sdB binary systems with very low mass companions. Some of these system even have companions in the brown dwarf (BD) mass regime. Since the sdB stars must lose their whole envelope during the CEE, those observations indicate that even very low mass companions are able to cause an envelope ejection. Schaffenroth et al. (2014) found two systems with minimum masses for the companion of $0.048\,\mathrm{M}_\odot$ and $0.027\,\mathrm{M}_\odot$, which puts both companions clearly below the hydrogen-burning limit.

Schaffenroth et al. (2017) further investigated close eclipsing sdB binaries (HW Vir systems) in the course of the the EREBOS (Eclipsing Reflection Effect Binaries form the OGLE Survey) project. They found several BDs orbiting sdB stars at very short orbital periods of 0.065 d to 0.096 d and concluded that more than 8 % of the close sdB systems might have sub-stellar companions. In Figure (1.2) the relationship between the companion mass and the period of known HW Vir systems is illustrated with an grey indication for the hydrogen burning limit. It makes clear that there have been many observations of light companion masses in the range between $0.1\,\mathrm{M}_\odot$ to $0.2\,\mathrm{M}_\odot$ and also several in the BD regime. The short periods show that theses systems are close binaries and imply that even though the companion's masses are low, they were sufficient to trigger the ejection of the RG progenitor's envelope.

In the later chapters of this work, we will endeavor to confirm via simulations whether low mass companions are indeed enough to eject the envelope of a RG, thus creating a sdB binary system.

2 Common Envelope Evolution

2.1 Introduction

As the name suggests, the CE refers to a short-lived phase in the evolution of a binary system when two stars are close enough to orbit in a single shared envelope. CEE plays an important role in the evolution of several major astrophysical phenomena such as type Ia supernovae, X-ray binaries and double NSs. It is thus directly connected to standard candles or gravitational wave sources.

Especially for the formation of compact binaries, CE evolution is widely seen as the mechanism responsible for shrinking the orbits. Many of the observed close binaries must have undergone a CE phase, as the progenitors of the compact objects were at some point orders of magnitude larger than the orbital distance of the current day system.

Even though many of the close binaries have no remainder of their CE, the ejection is not guaranteed. The exact physics of the CE phase are complex and still not fully understood. Gravitational drag during the spiral-in, instabilities and energy released by recombination are believed to be the driving mechanisms of the envelope unbinding.

In the following sections, we will summarize the most important parts of the CEE. We start with an overview of the different phases. Next, the energy budget and alpha formalism is explained, followed by the angular momentum transfer and ionization energy.

2.2 Main Phases

CEE is typically divided into several distinct phases, which proceed on their own time scale and are dominated by different physical phenomena. We will later endeavor to distinguish between some of those phases in our simulations, hence the following overview that is based on the review paper by Ivanova et al. (2013).

Loss of corotation

This phase sets in when the compact companion loses its synchronization with the gas particles of the donor stars' envelope and begins to spiral deeper into the CE. There are different mechanisms that could trigger this phase, e.g.:

- Dynamically unstable mass transfer, caused by an expansion of the donor star relative to its RL due to its proceeding evolution or as an reaction to mass loss.

- Natural formation of an CE, if the companion does not accrete transferred mass fast enough and the system is also unable to expel mass at a high enough rate. Matter will start filling out the binary orbit.

- Tidal instabilities.

This first phase of the CE evolution normally happens on the order of a dynamical timescale.

Plunge-in

The second stage is characterized by a fast spiral-in of the companion. The released orbital energy is deposited in the envelope, which drives its expansion and might lead to the unbinding and ejection of the envelope. Following Ivanova and Nandez (2016), we characterize this phase by an decay of the orbital separation A higher than 10 % over the course of a whole period P, thus:

$$\dot{A}P/A < -0.1 \tag{2.1}$$

This phase is dominated by dynamical interaction, especially gravitational drag. Under certain circumstances, the plunge-in can also be the last phase of the CE evolution, for example in case of a direct merger of the binary stars.

Self-regulating spiral-in

The third stage is initiated if the envelope expanded sufficiently during the plunge-in, so that the effect of the gravitational drag is weakened and the shrinking of the orbit becomes slower. The self-regulation is thought to be due to the effects of heating in the direct vicinity of the companion. If the density around the companion is low, frictional heating is inefficient, thus the material cools and the density rises again. In turn, this will increase friction and reheat the material and the cycle begins anew. Therefore, a regulated slow spiral-in occurs. Heating processes are decisive for this stage, making the thermal time scale the relevant one for the third phase.

Termination of the self-regulating phase

The phase is terminated by a complete ejection of the envelope by delayed dynamical ejection or other effects like the release of recombination energy, which typically only sets in after the plunge-in. The stage normally lasts several dynamical time-scales and a new CE phase might start if the companion or the remaining core of the primary evolves to a later stellar stage and expands.

Post-CE evolution

If the envelope is completely ejected, a close binary system remains. Its properties, for example eccentricity, can still be modified by the remaining circumstellar matter.

Stellar evolution of the remaining stars and its consequences, e.g. stellar winds can further change the binary system.

2.3 Energy Budget and Alpha Formalism

The standard way to describe CEE is based on a comparison between orbital energies before and after the event and the energy necessary to unbind the envelope completely, denoted as E_{bind} (Ivanova et al., 2013):

$$E_{\mathrm{bind}} = \Delta E_{\mathrm{orb}} = -\frac{G M_1 M_2}{2 a_{\mathrm{i}}} + \frac{G M_{\mathrm{c}} M_2}{2 a_{\mathrm{f}}} \tag{2.2}$$

The initial and final orbital separation is given by a_{i} and a_{f}, the initial mass of the primary star by M_1, the companion's mass by M_2 and the mass of the remaining core by M_{c}. Normally, one must assume that not all of the energy will be used to eject the envelope. Hence, a parameter α_{CE} is declared, that represents the CE efficiency and is defined as the fraction of the orbital energy used to unbind the envelope. This equation is often modified to account for the structure of the primary star by introducing a second parameter λ. The new parameter is a measure of how how strongly the envelope is bound to the core and is consequently strongly dependant on the definition of the core boundary transition. The adapted form of equation (2.2) yields

$$\frac{G M_1 M_{\mathrm{env}}}{\lambda R_1} = \alpha_{\mathrm{CE}} \left(\frac{G M_{\mathrm{c}} M_2}{2 a_{\mathrm{f}}} - \frac{G M_1 M_2}{2 a_{\mathrm{i}}} \right), \tag{2.3}$$

where R_1 is the radius of the primary and $M_{\mathrm{env}} = M_1 - M_{\mathrm{c}}$ the envelope mass. For most RGs, a value of $\lambda = 0.5$ seems to be adequate according to Dewi and Tauris (2000). This parametrization has been successfully employed to describe post-common envelope systems and is often used in population synthesis models. It should be mentioned that the definition also has some caveats, e.g. it is actually only valid if the whole envelope is ejected and additional energy sources like recombination energy are not considered. Including further energy sources can lead to counter-intuitive efficiency values larger than one.

2.4 Angular Momentum

In some cases, the formalism described in the last chapter fails to yield reasonable values for alpha, for example for a system of double helium WDs (Nelemans, 2000), where mass transfer can be connected to a widening of the orbit. Therefore, a second description based on the conservation of angular momentum is introduced:

$$\frac{\Delta J}{J} = \gamma \frac{\Delta M}{M} \tag{2.4}$$

Here, the angular momentum is given as J, the mass as M and $\Delta J, \Delta M$ describe the changes in the respective measure. The new parameter γ adopts values in the range between 1.4 and 1.7 for the system that were analyzed.
Expressing the orbital Energy E_{orb} of a binary in terms of its angular momentum J, its eccentricity e, its total mass M and the reduced mass μ yields interesting insights for the dynamical plunge-in at the beginning of CEE:

$$E_{\mathrm{orb}} = -\frac{G^2 M^2 \mu^3 \left(1 - e^2\right)}{2J^2} \tag{2.5}$$

Considering the limit of the regime at the very beginning of the spiral-in, when the orbital Energy is almost constant $\mathrm{d}E_{\mathrm{orb}} \approx 0$, we can infer

$$\frac{de^2}{1 - e^2} \approx -2\frac{dJ}{J}. \tag{2.6}$$

The equation implies that at the start, the binary's eccentricity should grow approximately as fast as angular momentum J is transferred to the envelope.
The orbit can be expected to circularize after the condition $a/R \lesssim r_{\mathrm{g}}^{4/3}$ is met, where the radius of the CE is denoted as R and the dimensionless gyration as r_g (relation to the moment of inertia: $I = r_{\mathrm{g}}^2 M R^2$). For giants the gyration adopts values of $r_g^2 \approx 0.1$.

2.5 Ionization Energy

Recent works have shown the importance of ionization energy for CEE, especially with respect to the possible unbinding of the envelope (Ivanova, 2018; Nandez et al., 2015). If the gas of the envelope expands, cools down and transits from ionized to neutral matter, large quantities of energy can be released. This so called recombination energy drives the ejection of the envelope.
The following treatment is based on Kippenhahn (2012). In the envelope, the main contributions to the ionization energy is due to hydrogen and helium. Thus, there are five types of particles, namely {H, H$^+$, He, He$^+$, He^{++}} plus the respective electrons. The corresponding ionizations energies are denoted as χ^0_{He} for hydrogen and $\chi^0_{\mathrm{He}}, \chi^1_{\mathrm{He}}$ for neutral and single ionized helium. The internal energy of the gas is increased by $\chi^0_{\mathrm{H}} = 13.598\,\mathrm{eV}$ for each single ionized hydrogen atom, by $\chi^0_{\mathrm{He}} = 24.587\,\mathrm{eV}$ for each single ionized helium and by $\chi^1_{\mathrm{He}} = 54.418\,\mathrm{eV}$ for each double ionized helium atom. We define x_i^r as the number of atoms of type i in ionization state r divided by the total number of atoms of type i

$$\begin{aligned} x^0_{\mathrm{H}} = \frac{n^0_{\mathrm{H}}}{n_{\mathrm{H}}},\ x^1_{\mathrm{H}} = \frac{n^1_{\mathrm{H}}}{n_{\mathrm{H}}}, \quad x^0_{\mathrm{He}} = \frac{n^0_{\mathrm{He}}}{n_{\mathrm{He}}} \\ x^1_{\mathrm{He}} = \frac{n^1_{\mathrm{He}}}{n_{\mathrm{He}}}, \quad x^2_{\mathrm{He}} = \frac{n^2_{\mathrm{He}}}{n_{\mathrm{He}}} \end{aligned} \tag{2.7}$$

where $n_{\mathrm{H}} = n^0_{\mathrm{H}} + n^1_{\mathrm{H}}$ and $n_{\mathrm{He}} = n^0_{\mathrm{He}} + n^1_{\mathrm{He}} + n^2_{\mathrm{He}}$ with the number densities of ions of type i in ionization state r given as n^r_i. Generally, the contribution of the ionization energy to the specific internal energy is defined as:

$$u_{\mathrm{ion}} = \sum_i \frac{X_i}{\mu_i m_{\mathrm{u}}} \sum_{r=0}^{Z_i} x^r_i \sum_{s=0}^{r-1} \chi^s_i \tag{2.8}$$

Here, X_i is the mass fraction of element i and m_u the atomic mass number. For a mixture of helium and hydrogen, the general equation (2.8) simplifies to

$$u_{\mathrm{ion}} = \frac{1}{m_{\mathrm{u}}} \left\{ X x^1_{\mathrm{H}} \chi^0_{\mathrm{H}} + \frac{1}{4} Y \left[x^1_{\mathrm{He}} \chi^0_{\mathrm{He}} + x^2_{\mathrm{He}} \left(\chi^0_{\mathrm{He}} + \chi^1_{\mathrm{He}} \right) \right] \right\}, \tag{2.9}$$

with the X and Y referring to the chemical mass fractions for hydrogen and helium. We include ionization energy in all of our later simulations by applying the OPAL equation of state (Rogers and Nayfonov), that uses pre-computed tables to interpolate the opacities from the temperature and density values.

3 Numerical Methods

3.1 AREPO

The simulations presented and evaluated in the later course of this thesis are all based on the AREPO code described in Springel (2010). The code combines the advantages of both smoothed particle hydrodynamics (SPH) and static grid codes. This is achieved by solving the Euler equations with a finite volume method on a moving unstructured mesh. The possibility to arbitrarily move the mesh generating points guarantees almost Lagrangian behavior, hence ensuring Galilean invariance. The unstructured grid uses the approach of the Voronoi tesselation of space for a given set of mesh-generating points. All points in space that are nearest to a mesh-generating point are thereby assigned to a corresponding Voronoi cell, that defines a finite volume for the hydrodynamic treatment. Thus, in contrast to pure SPH codes, shocks and discontinuities can be calculated with high precision. The resolution can be controlled by simple criteria that determine when cells get redefined, which is known as adaptive mesh refinement (AMR). For example, we apply a criterion to refine a cell if its mass surpasses a predefined threshold.

The different steps executed by AREPO can be described in the following way: First, initial conditions are loaded and a domain decomposition is carried out. Next, the gravitational forces and the Voronoi mesh are determined. Then, a new time step and the first gravitational half-kick are calculated, followed by gradients, vortex velocities and hydro flux. The cell refinement and new particle assignation is executed. Now, the time bins are updated and only relevant particles for the next step are selected before starting the second gravitational half-kick. Finally, the OPAL equation of state (EOS) is applied in a tabular way on the temperature-density grid and interpolated.

3.2 Finite Volume Hydrodynamics

The following section is based on Springel (2010) and contains a short description of the hydrodynamic equations and how they are discretized in AREPO to allow numerical calculation of solutions. The Euler equations constitute a set of hyperbolic partial differential equations that govern the properties of hydrodynamic flows. They represent conservations laws for mass, momentum and energy.

In accordance with Springel (2010), we will use the compact form by introducing the state vector

$$\boldsymbol{U}(\boldsymbol{x},t) = \begin{pmatrix} \rho \\ \rho\boldsymbol{v} \\ \rho e \end{pmatrix} = \begin{pmatrix} \rho \\ \rho\boldsymbol{v} \\ \rho u + \frac{1}{2}\rho\boldsymbol{v}^2 \end{pmatrix} \tag{3.1}$$

to describe the fluid, where ρ is the mass density, $\boldsymbol{v}$ is the velocity field, $e = u + \boldsymbol{v}^2/2$ is the total energy per unit mass with u denoting the thermal energy per unit mass. For an ideal gas, the thermal energy only depends on temperature. To simplify the notation, we will omit the explicit dependence of $\boldsymbol{U}$ from the spatial coordinate $\boldsymbol{x}$ and the time t.

The flux of the fluid is given by

$$\boldsymbol{F}(\boldsymbol{U}) = \begin{pmatrix} \rho\boldsymbol{v} \\ \rho\boldsymbol{v}\boldsymbol{v}^T + \boldsymbol{P} \\ (\rho e + \boldsymbol{P})\boldsymbol{v} \end{pmatrix} \tag{3.2}$$

and the equation of state

$$P = (\gamma - 1)\rho u \tag{3.3}$$

describes the pressure with the adiabatic index γ. This allows us to write the Euler equations in the concise form

$$\frac{\partial \boldsymbol{U}}{\partial t} + \nabla \cdot \boldsymbol{F} = 0, \tag{3.4}$$

which makes their nature as conservation of mass, momentum and energy apparent. The set of equation must now be discretized to allow numerical solutions of the hydrodynamic flow, which is achieved by solving an Riemann problem at cell boundaries based on Godunov's method. The discretization is performed by subdividing the system's volume into a finite number of disjoint cells. The fluid's state is given by the average of the conserved quantities within each cell. Hence, we obtain the total mass m_i, momentum $\boldsymbol{p_i}$ and energy E_i of a specific cell i by integrating $\boldsymbol{U}$ over the cell's volume V_i:

$$\boldsymbol{Q}_i = \begin{pmatrix} m_i \\ \boldsymbol{p}_i \\ E_i \end{pmatrix} = \int_{V_i} \boldsymbol{U} \mathrm{d}V \tag{3.5}$$

Applying Gauss' theorem to convert the volume integral to a surface integral over the boundaries enables us to determine the rate of change of $\boldsymbol{Q_i}$ in time

$$\frac{\mathrm{d}\boldsymbol{Q}_i}{\mathrm{d}t} = -\int_{\partial V_i} \left[\boldsymbol{F}(\boldsymbol{U}) - \boldsymbol{U}\boldsymbol{w}^T\right] \mathrm{d}\boldsymbol{n}, \tag{3.6}$$

where $\boldsymbol{n}$ is the normal vector on the cell surface pointing outward and $\boldsymbol{w}$ gives the velocity with which each point of the cell boundary moves. In typical Eulerian codes, a static grid is utilized which means that $\boldsymbol{w} = 0$. In contrast, a fully Lagrangian code would imply $\boldsymbol{w} = \boldsymbol{v}$, thus simplifying the integral term of the equation, as the mass stays constant for each cell. However, strong distortions of the fluid volumes can not be followed and hence limit the simulation time for which the Lagrangian approach is feasible. Because AREPO uses a moving mesh, the general form of equation (3.6) must be solved. Volumes are subdivided in polyhedra with flat polygonal surfaces. Therefore, the flux between two adjacent cells i and j can be described by

$$\boldsymbol{F}_{ij} = \frac{1}{A_{ij}} \int_{A_{ij}} \left[\boldsymbol{F}(\boldsymbol{U}) - \boldsymbol{U}\boldsymbol{w}^T\right] \mathrm{d}\boldsymbol{A}_{ij} \tag{3.7}$$

where $\boldsymbol{A}_{ij}$ is the oriented area between cells i and j (pointing from the first to the latter). The Euler equations change into

$$\frac{\mathrm{d}\boldsymbol{Q}_i}{\mathrm{d}t} = -\sum_j A_{ij}\boldsymbol{F}_{ij} \tag{3.8}$$

for the finite-volume approach. A time discretization can be written as

$$\boldsymbol{Q}_i^{(n+1)} = \boldsymbol{Q}_i^{(n)} - \Delta t \sum_j A_{ij}\hat{\boldsymbol{F}}_{ij}^{(n+1/2)} \tag{3.9}$$

with the time-averaged flux across the cell face $\hat{\boldsymbol{F}}_{ij}$ and the state of the system at n-th time step $\boldsymbol{Q}_i^{(n)}$. To determine the fluxes $\hat{\boldsymbol{F}}_{ij}$, AREPO employs Godunov's method which has a second-order accuracy in space and time. Inside each cell, it applies a slope-limited piece-wise linear reconstruction step, followed by a first order prediction step for the evolution over half a time-step and finally a Riemann solver to estimate the time-averaged inter-cell flux.

3.3 Gravity in AREPO

If a gravitational field is present, the Euler equations discussed in the previous section need to be modified by source terms for momentum and energy. The most obvious approach

$$\frac{\partial \boldsymbol{U}}{\partial t} + \nabla \cdot \boldsymbol{F} = \begin{pmatrix} 0 \\ -\rho\nabla\Phi \\ -\rho\boldsymbol{v}\nabla\Phi \end{pmatrix} \tag{3.10}$$

with the gravitational potential Φ, that describes self gravity as a solution of the Poisson's equation

$$\nabla^2\Phi = 4\pi G\rho \tag{3.11}$$

leads to the following discretized description for the total energy of the cell i:

$$E_\mathrm{i} = \int_{V_i}\left(\rho e + \frac{1}{2}\rho\Phi\right)\mathrm{d}V. \tag{3.12}$$

The detailed steps describing the necessary changes to equation (3.9) can be found in Springel (2010), but for this work, the qualitative description suffices.
The self-gravity of the gas in AREPO is implemented with a tree-algorithm, that was adopted from the predecessor code GADGET-2 (Springel, 2005). Furthermore, AREPO applies gravitational softening when calculating the potentials and forces in order to avoid numerical divergences for close encounters of particles. Instead of accounting for the precise form of each of the cells, AREPO represents the potential of each gas cell with a top-hat sphere of the radius h. For improved smoothness, the volume of the spheres is chosen to be slightly larger than the cell volume itself with the relation $h = f_h(3V/4\pi)^{1/3}$ and $f_h \approx 1.0$-1.5. The kernel for the gravitational potential of a cell of the volume V is given by

$$\phi(r,h) = -\frac{1}{r}\begin{cases} \frac{r}{2h}\left[3 - \left(\frac{r}{h}\right)^2\right] & \text{for } r \leq h \\ 1 & \text{for } r > h \end{cases} \tag{3.13}$$

which leads to the following total gravitational self-energy for a system of Voronoi cells:

$$E_\mathrm{pot} = \frac{1}{2}\sum_{ij} G m_i m_j \phi\left(r_{ij}, h_j\right) \tag{3.14}$$

3.4 Simplifications

The simulations presented in this thesis do not include magnetic fields. This, however, should not have a big impact on the dynamics of the CE physics, as pointed out by Ohlmann et al. (2016). It was shown that even though magnetic field amplifications took place, the resulting field strength were too small to be dynamically relevant.
Energy generation by nuclear burning is also neglected in the simulations, since the timescales of the spiral-in of the CE phase happens on a much smaller timescale than both the nuclear and the radiation transport timescale.

4 Initial Models

The AREPO code was developed with the aim to conduct cosmological simulations. Consequently, we need to change the initial conditions for our simulation runs to adapt the code to the scale and context of the CEE. This means that we need a model for the primary star that is adequately evolved to emulate a RG star. The first section describes how we obtain such a model by using the stellar evolution code MESA. Afterwards, some more technical steps of the subsequent relaxation of the star on the three dimensional grid of AREPO are explained. Finally, we present the result of the process.

4.1 Mesa Profiles

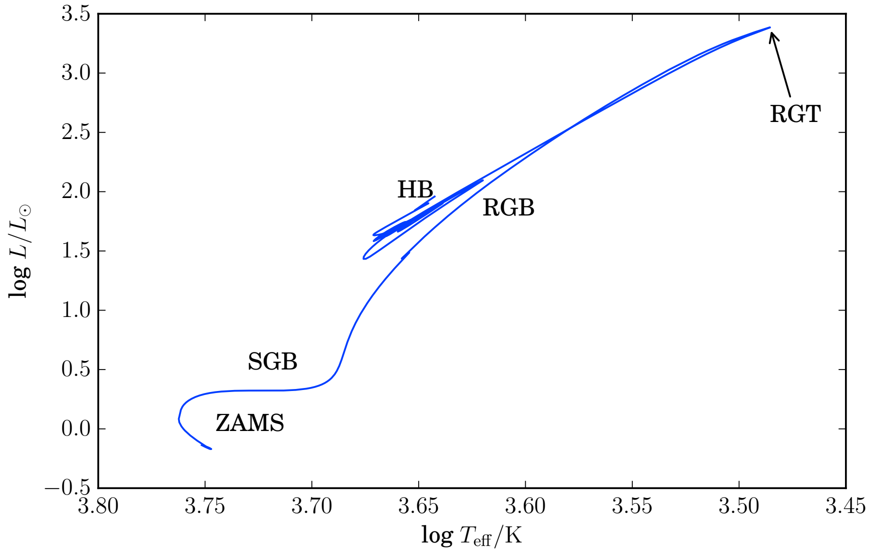

Figure 4.1: Evolutionary track of a one solar-mass star simulated by MESA. Different stages are annotated as ZAMS: Zero age main sequence, SGB: Subgiant branch, RGB: Red giant branch, RGT: Tip of the red giant branch and HR: Horizontal branch. We use the profile right at the tip of the RGB as our progenitor for the AREPO runs.

For the simulations of the CEE via AREPO, initial condition for the binary system are necessary. As this work focuses on evolution of sdB stars, we require a setup with a star at the red giant tip as initial model (Section 1.2). In order to achieve this, the stellar evolution code MESA (Paxton et al., 2013, 2015) is used with a stopping condition on the helium burning. The simulated model has a metallicity of $Z = 0.02$ and uses the Reimers prescription with $\eta = 0.5$ for RG winds. We evolve a star with zero age main sequence (ZAMS) mass of $1\,\mathrm{M}_\odot$. In Figure (4.1), the HR diagram of the MESA run is plotted. We chose the profile right at the tip of the RG branch for our initial mapping procedure to AREPO. At this point, the core mass accounts to $0.47\,\mathrm{M}_\odot$ and the envelope mass to $0.30\,\mathrm{M}_\odot$, which is well suited to represent a sdB progenitor star (Chapter 1).

4.2 Relaxation

Since the initial stellar profile obtained from the MESA code is one-dimensional, we need to map it to a three-dimensional grid in order to use it with AREPO. This causes several problems, as discretization errors are introduced by the mapping process. Moreover, AREPO has different discretizations for the pressure gradient and the gravitational force gradient, hence they do not cancel each other out exactly. This generates spurious velocities within the star and the necessity for a relaxation procedures arises. This work follows the relaxation process described in detail **?** and only the main points and the results are presented in this section.

As shown in **?**, both spatial and temporal scales in RG are of such great differences, that it is not feasible to simulate them in a reasonable amount of time. Therefore, certain approximations have to be made: the core of the giant is replaced by a point particle that only interacts gravitationally and a modified Lane-Emden equation is applied to achieve a suitable transition between core and envelope that represents the initial stellar model with a high enough accuracy.

Conveniently, particles that only interact gravitationally are already implemented in AREPO for modeling dark matter (DM) in cosmological simulations. Henceforth, we will refer to them as DM particles. The corresponding gravitational acceleration is described by the following spline function:

$$g_\mathrm{c}(r) = -Gm_\mathrm{c}\frac{r}{h^3}\begin{cases} -\frac{32}{3} + u^2\left(\frac{192}{5} - 32u\right), & 0 \leq u < \frac{1}{2} \\ \frac{1}{15u^3} - \frac{64}{3} + 48u & \\ -\frac{12}{5}u^2 + \frac{32}{3}u^3, & \frac{1}{2} \leq u < 1 \\ -\frac{1}{u^3}, & u \geq 1 \end{cases} \tag{4.1}$$

Here h is the softening length of the interaction, m_c is the mass of the core particle and u is defined as $u = r/h$. The equation of hydrostatic equilibrium is adapted to account for the newly introduced core

$$\frac{\mathrm{d}p(r)}{\mathrm{d}r} = -G\frac{m(r)\rho(r)}{r^2} - \rho(r)g_\mathrm{c}(r) \tag{4.2}$$

The pressure, radius, mass and density are given by p, r, m and ρ respectively. **?** demonstrated that the scaling of equation (4.2) compared to the unmodified one stays the same when expanded into a series around $r = 0$. Considering the radial mass profile of giants, almost constant mass over large scales of relevant radii are observed, which shows that the core is very compact in contrast to a quite dilute envelope. Consequently, replacing the core by a DM particle is well justified if the mass profile is cut off in its flat regime.

? next introduce a modified Lane-Emden equation by combining the adapted pressure equation (4.1) with the conservation of mass:

$$\frac{\mathrm{d}m(r)}{\mathrm{d}r} = 4\pi r^2 \rho(r). \tag{4.3}$$

This allows us to obtain a continuation of the stellar profile from the cut inwards, so that in the end a complete smooth profile from the center to the outer envelope can be generated, that represents the original with satisfying accuracy. The detailed steps of this derivation can be found in **?**.

As pointed out above, the mapping process of the one-dimensional MESA profile to a three-dimensional grid might give rise to unstable atmospheres and spurious velocities. In order to stabilize these numerical artifacts, damping is applied to smooth out fluctuations. To that effect, the following term is added to the momentum equation

$$\dot{\boldsymbol{v}} = -\frac{1}{\tau}\boldsymbol{v} \tag{4.4}$$

which has the solution

$$\boldsymbol{v}(t) = \boldsymbol{v}_0 \exp\left(-\frac{t}{\tau}\right) \tag{4.5}$$

where $\boldsymbol{v}$ is the velocity and τ the damping time scale. Especially for giants, which have very low densities in their outer parts, the value of τ plays an important role to reach a stable star. Following **?**, we chose a total simulation time of ten dynamical timescales t_{dyn}. The damping is then gradually reduced according to the following scheme

$$\tau(t) = \begin{cases} \tau_1, & t < 2t_{\mathrm{dyn}} \\ \tau_1 \left(\frac{\tau_2}{\tau_1}\right)^{\frac{t-2t_{\mathrm{dyn}}}{3t_{\mathrm{dyn}}}}, & t < 5t_{\mathrm{dyn}} \\ \infty, & t > 5t_{\mathrm{dyn}} \end{cases} \tag{4.6}$$

with $\tau_1 = t_{\mathrm{dyn}}/10$ and $\tau_2 = t_{\mathrm{dyn}}$. This means that the damping is effectively turned off after half the time of the relaxation run has passed. The system evolves further for $5t_{\mathrm{dyn}}$ to guarantee that it stays stable without damping.

Since this procedure does technically not enforce hydrostatic equilibrium with $\nabla p =$

$-\rho\nabla\Phi$, changes in the profile of the hydrostatic equilibrium are possible and relaxation runs should be checked for close resemblance with the original profile.

4.3 Simulation and Results

We applied the relaxation procedure (Chapter 4.2) to the Mesa profile of a $1\,\mathrm{M}_\odot$ ZAMS star at the tip of the RGB. The box size of the computational domain amounted to $1409\,\mathrm{R}_\odot$ and the simulation time was set to $911\,\mathrm{d}$, which corresponds to ten dynamical timescales (Section 4.2). We further impose a resolution of 3.1×10^6 initial cells.

In Figure (4.2), the quality of the hydrostatic equilibrium in the star at different points of time during the relaxation run is shown. The upper panel compares the pressure gradient to the gravitational potential. Ideally, both lines should match each other, but as pointed out in Section (4.2), this is by no means trivial. The blue line shows both gradients at the beginning of the simulation. Here, the routine explained in Chapter (4.2) was applied to obtain the initial three-dimensional setup from the one-dimensional MESA profile. During the course of the simulation, we observe a gradual smearing out of the outer edge of the star, but a good general agreement between both gradients. The lower panel in Figure (4.2) displays the relative deviation between pressure gradient and gravitational potential. It shows very good agreement in the inner parts of the star where the deviation for the end of the simulation at $t = 911\,\mathrm{d}$ is around 2×10^{-2}. The outer areas close to the star's surface show larger deviations due to the expansion. Since there is only very little mass in the outer areas, the star is still in a reasonably good hydrostatic equilibrium and no mass outflow is observed.

In Figure (4.3), the Mach number is plotted at different times during the relaxation run. We note that there is no rise in the Mach number after the damping is turned off after half the simulation time and that it is generally rather low, except for the dilute surface area. In the same plot in the lower panel, the density profile at different times is shown. The initial profile at $t = 0$ d is determined from the MESA profile as described in Section (4.2). The time evolution shows a gradual smearing out of the sharp edge of the density, but very little deviation for the inner parts where density is much higher and most of the mass is situated. While the smearing out is not desirable, all of the mass is still bound and no outflow is observed.

At the end of the relaxation, we obtain a star with an DM core of the mass $M_\mathrm{c} = 0.47\,\mathrm{M}_\odot$ and an envelope gas mass of $M_\mathrm{env} = 0.30\,\mathrm{M}_\odot$. This results in a total mass of $M_\mathrm{tot} = 0.77\,\mathrm{M}_\odot$. As we started with a MESA profile of $M_\mathrm{tot} = 1\,\mathrm{M}_\odot$, we register a mass loss of $M_\mathrm{ej} = 0.23\,\mathrm{M}_\odot$. However, this mass loss takes place during the evolution of the star on the RGB due to stellar winds and not during the relaxation. In conclusion, we are left with a relaxed star whose evolutionary stage is right at the tip of the RGB with a core mass typical for sdB stars. We are thus equipped to set-up a binary system in the next step and check how effectively envelope mass is ejected to infer more information about the CE formation channel of sdB stars.

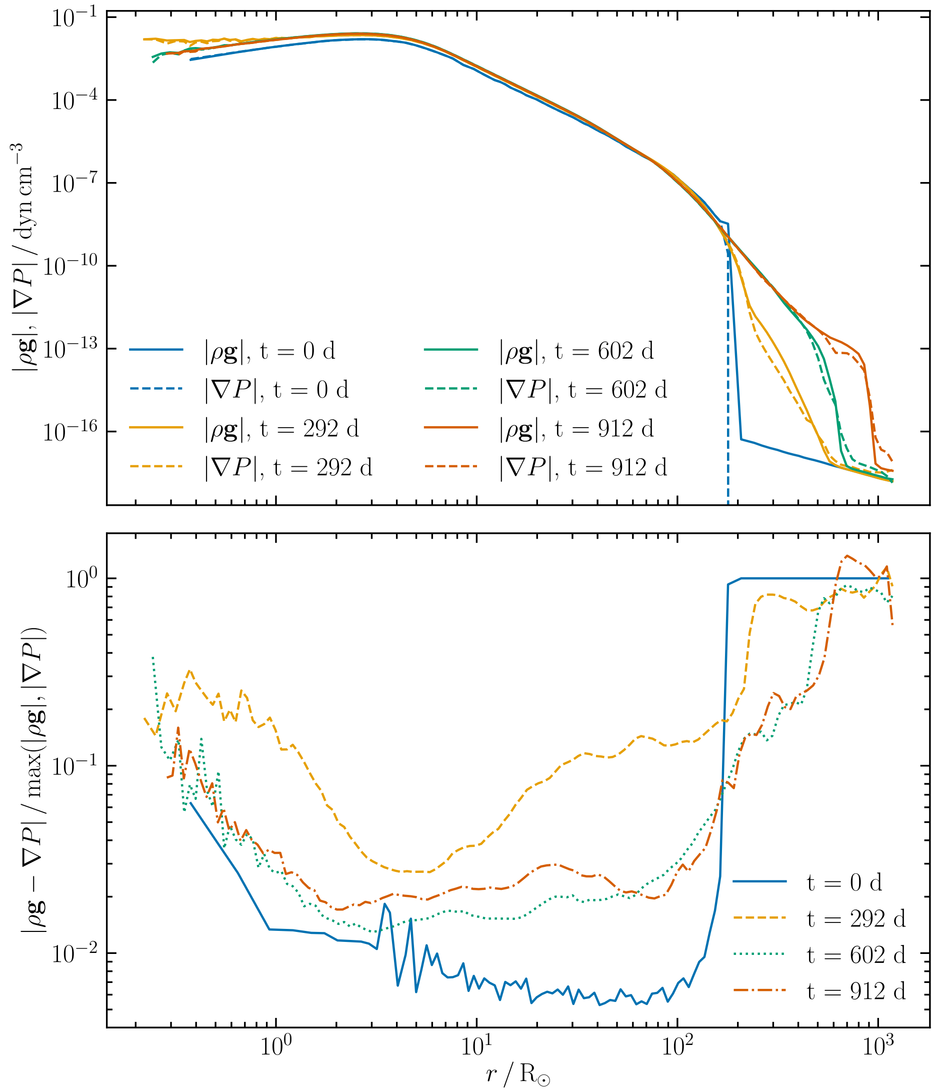

Figure 4.2: Hydrostatic equilibrium for the relaxation run at different times. In the top panel, both pressure gradient (dashed line) and gravitational potential (solid line) are plotted. The lower panel depicts the deviation from the hydrostatic equilibrium. The blue line for $t = 0\,\mathrm{d}$ is derived from the initial MESA profile, as described in Section (4.2).

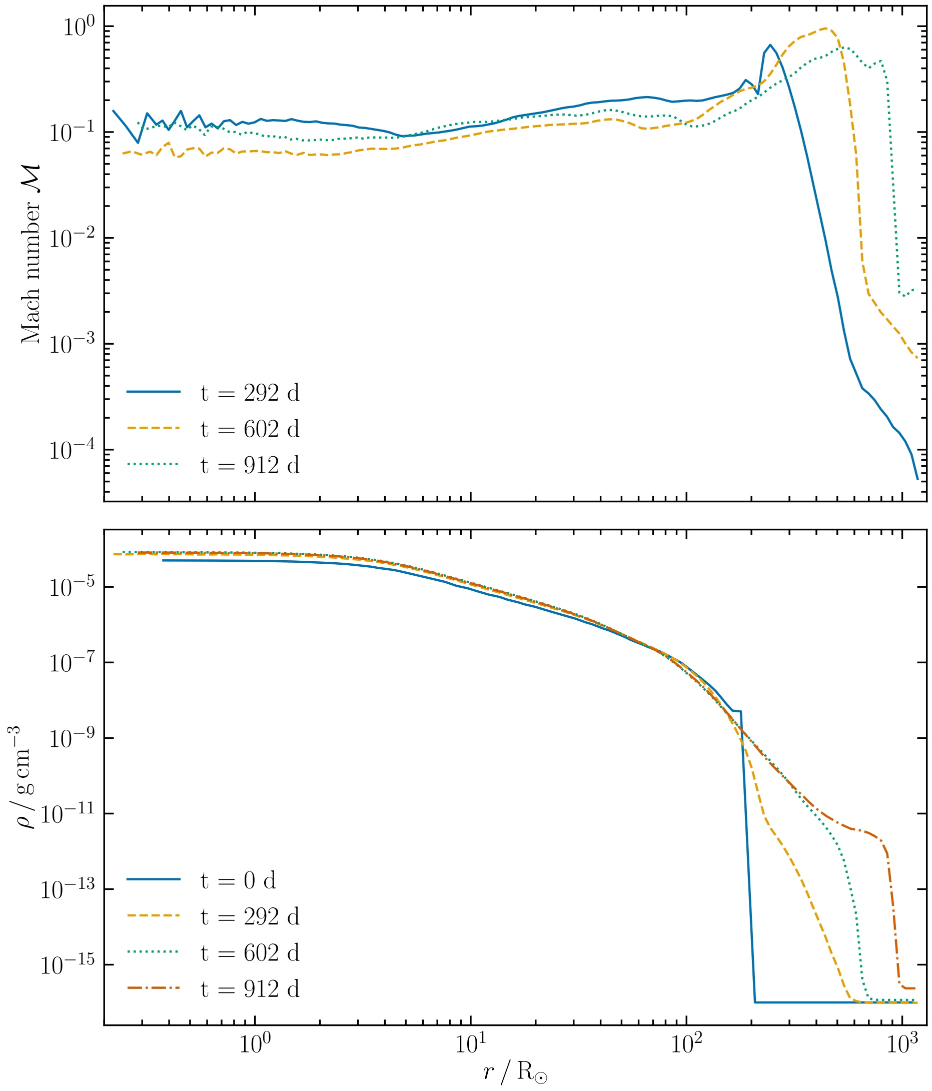

Figure 4.3: Mach number and density profile for the relaxation run at different times. The upper panel shows the Mach number over the radius. The lower panel illustrates the density profile of the star.

5 A First Common Envelope Simulation with a Light Companion

In this section, a first hydrodynamic simulation of the spiral-in and the ensuing CE phase is presented. The moving mesh code AREPO is used to follow the evolution of a binary system that consists of a $0.77\,\mathrm{M}_\odot$ RG at the tip of the RG branch and a compact companion with a mass of $0.1\,\mathrm{M}_\odot$.

5.1 Setup

In the following chapter, the details of a set-up of a first CE simulation with a RG and a point sized companion are described. We use the moving mesh code AREPO (Springel, 2010) to follow the evolution of a binary system with a $0.77\,\mathrm{M}_\odot$ RG at the tip of the RG branch and a compact companion with $0.1\,\mathrm{M}_\odot$. We thus have a very small mass ratio of almost 1/8, which is much lower than comparable previous simulations used. The RG primary was obtained by using the stellar evolution code MESA (Paxton et al., 2013, 2015) with an ZAMS mass of $1\,\mathrm{M}_\odot$. Following the procedure described in Chapter (4), the MESA model is first evolved until the star reaches the tip of the RGB and then mapped to a three-dimensional grid. To remove numerical artifacts caused by the mapping, a relaxation run is conducted to stabilize the stellar model (Section 4.2). After the relaxation, we obtain a stable star with a core mass of $0.47\,\mathrm{M}_\odot$ and an envelope mass of $0.30\,\mathrm{M}_\odot$. Both the stage of the star at the tip of the RGB and the core mass that lies in the mass regime of sdB stars make this set-up well suited to gain insight into the formation process of sdB stars via CEE (Section 1.2).

We chose periodic boundary conditions and a cubic computational domain of the size $1.1 \times 10^{16}\,\mathrm{cm}^3$ to ensure that no significant amount of mass can reach the edge of the computation domain within the simulation time.

The binary system was set up by placing the RG star from the relaxation run on a three-dimensional grid and substituting the high density core with a DM particle that only interacts gravitationally. For the compact companion star a second DM particle without a gaseous atmosphere is introduced, which is placed at an initial distance that corresponds to 80 % of the RLOF distance ($157.4\,\mathrm{R}_\odot$), which is well outside the radius of the RG primary ($110\,\mathrm{R}_\odot$). Consequently, the simulation also tracked the first phase of the CE evolution, the plunge-in. This could be further improved by placing the companion directly at the RLOF distance to fully account for the transfer of energy and angular momentum from the orbit to the envelope. Moreover, the structure of the primary would be kept in better equilibrium by placing the companion further out. Unfortunately, the necessary computational cost also rises considerably, since reaching the plunge-in phase would require much more time. The x- and y-coordinates of the companion were set identical to those of the RG core. The gravitational force of the DM particles is smoothed according to the spline function given in Springel (2010) on a length of $h = 2.4 \times 10^9\,\mathrm{cm}$.

The initial velocity of the companion star is set in such a way that its corotation frequency matches the Keplerian frequency. The velocity of the envelope is chosen asynchronously by imposing a corotation factor of 0.95.

We employ two refinement criteria for this simulation: The grid is refined to obtain a certain target mass - if a cell's mass surpasses twice the target mass, it will be refined. The target cell mass was set to $1.4 \times 10^{-7}\,\mathrm{M}_\odot$. In addition, in the area close to the point particles, a second criterion is applied. As soon as the distance to a point mass is less than five softening lengths, a cell will be refined if its radius is larger than the softening length divided by 40. We will show later that this proves to be sufficient to resolve the interaction between pressure and gravity to a very high accuracy.

The total number of cells used initially accounts to 2.4×10^6 and at the end of the simulation to 3.3×10^6. This yields an average initial cell mass of $1.8 \times 10^{-7}\,\mathrm{M}_\odot$ and $1.1 \times 10^{-7}\,\mathrm{M}_\odot$ for the final average cell mass due to the additional cells created through the refinement criteria. Moreover, we impose that that the softening length of the point masses always stays below the distance between companion and RG core to ensure that the gravitational interaction between both particles is never softened.

Recent findings in the CE physics suggest that recombination energy plays an important role in the unbinding of the envelope (Nandez et al., 2015; Ivanova, 2018), even though it is still under discussion how much of the released energy by recombination will be used to eject the envelope. Our simulations take recombination energy into account by applying the OPAL EOS (Rogers and Nayfonov), that is coupled to the hydrodynamics scheme. An additional iterative solver computes thermodynamic quantities from pre-calculated tables according to the OPAL EOS.

5.2 Results and Discussion

In Figure (5.2), the evolution of the distance between the two point masses is plotted. During the initial 60 d, the distance stays almost constant, while the companion slowly starts to accrete mass from the diffuse envelope material. After 60 d, the companion enters a phase of rapid spiral-in toward the center of the binary system, that is characterized by an orbital decay rater higher than 10 % (Section 2.2). At $t = 550\,\mathrm{d}$, the plunge-in comes to a halt at a separation of about $23\,\mathrm{R}_\odot$. There is only little mass left within the orbit, namely 6.8 % of the envelope mass, which explains the subsequent stabilization of the orbit. The companion enters a quiet phase of slow orbital decay. Until $t = 800\,\mathrm{d}$, the orbit decreases to a separation of $14\,\mathrm{R}_\odot$ and in the last hundred days of the simulation, it only shrinks by $0.22\,\mathrm{R}_\odot$ to

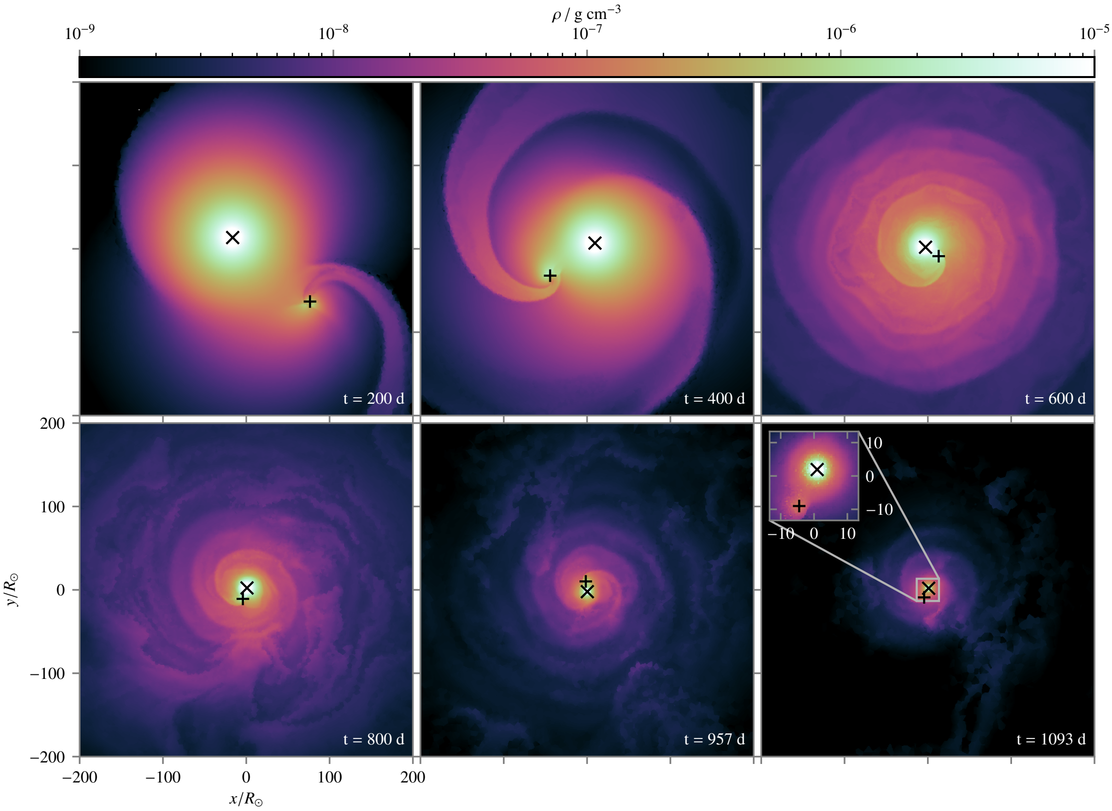

Figure 5.1: Time series of density snapshots in the x-y plane at six different times. The positions of the cores of the RG primary and the companion are marked by an × and + respectively. Each frame is centered on the center of mass of the binary system. The inset in the last panel zooms in on the central square region with an edge length of $20\,\mathrm{R}_\odot$ with a color scale comprising values from 10^{-5} to 10^{-8} $\mathrm{g\,cm^{-3}}$.

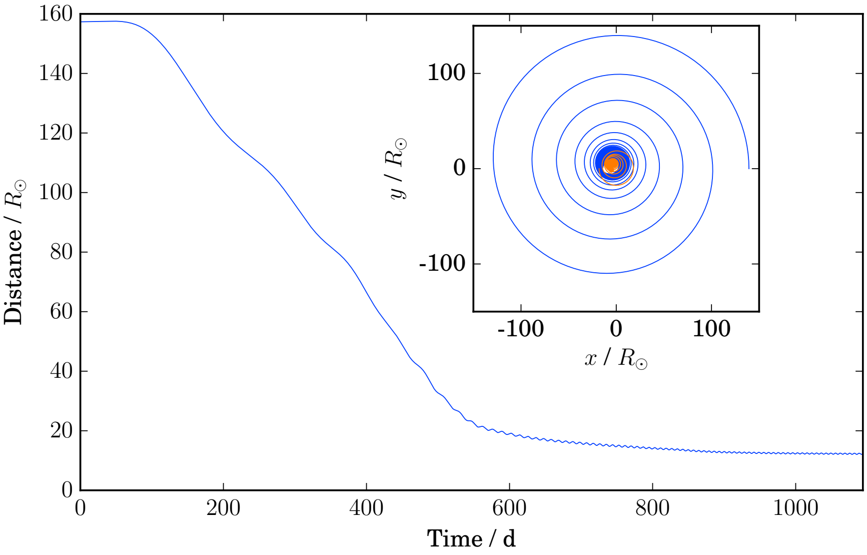

Figure 5.2: Evolution of the separation between point particles and orbital trajectories. The main panel displays the distance between the two point particles during the simulation time. The inset shows the position of companion's core in blue and the position of the core of the RG in red.

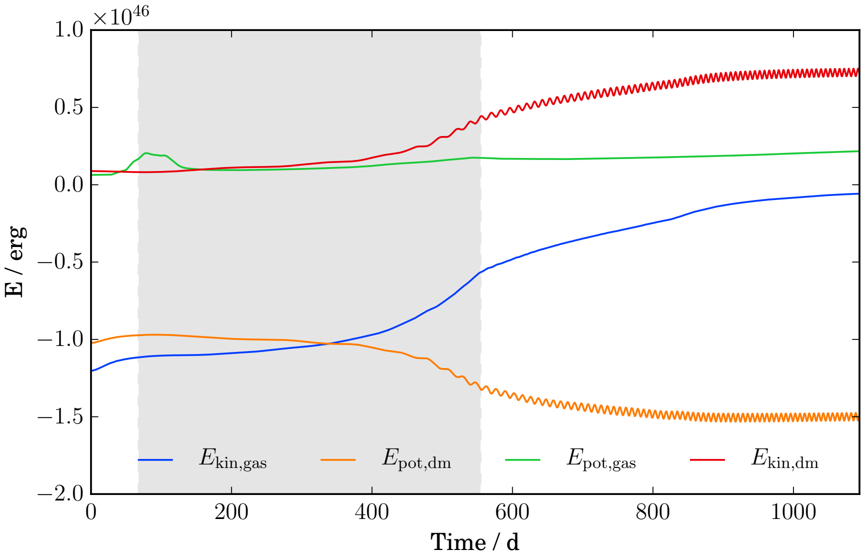

Figure 5.3: Overview of the potential and kinetic energy of the DM particles and the gas particles of the envelope. The gray area indicates the plunge-in phase.

a final value of $12\,\mathrm{R}_\odot$. The remaining enclosed mass is further reduced to a bare $0.08\,\%$ at the end of the simulation, thus all of the mass is already outside the orbit and dynamic interactions are smothered. We would not expect further spiral-in and a stable orbit is reached.

The inset of Figure (5.2) shows the orbital trajectories of the companion and the core of the RG in blue and red respectively. Since the mass of the companion is low, the movement of core of the RG is rather small compared to the companion. While the orbit is initially quite eccentric with an eccentricity of $e = 0.43$ at $t = 100\,\mathrm{d}$, it is already much more circularized at the end of the spiral-in with $e = 0.10$. The final values amounts to $e = 0.016$. Over the course of the simulation, the orbital period evolves from a value of $303\,\mathrm{d}$ at the start to $6.6\,\mathrm{d}$ at the end.

In Figure (5.1), snapshots of the density in the x-y plane are shown at different times of the simulation run, illustrating the dynamics of the binary interaction. The positions of the core of the RG and the companion are denoted by an × and + respectively. The first two panels show a tidal accretion stream being formed. Between the first and the second panel, the companion is in the phase of rapid plunge-in and the separation to the RG core decreases substantially. The outer layer of the RG primary is disrupted by the trajectory of the companion, which results in a region of low density between the extended tidal arm and the inner regions of the RG star. In the course of the subsequent orbits, spiral shock waves moving outwards lead to a layered structure around the RG core. Between adjacent layers, instabilities emerge and start disrupting the concentric shapes of the different layers. Especially the outer parts shown in the fourth panel show turbulent behavior. In the last panels of Figure (5.1), the structure has lost a lot of its regular shape and the density has decreased significantly. The layered structure is supplanted by large-scale instabilities.

The energy budget for potential and kinetic energy of the cores and the envelope gas can be seen in Figure (5.3). During the whole simulation, the potential energy of the cores is raised from $-1.02 \times 10^{46}\,\mathrm{erg}$ to $-1.5 \times 10^{46}\,\mathrm{erg}$, while the potential energy of the gas increases by $1.1 \times 10^{46}\,\mathrm{erg}$, which corresponds to a change of $95\,\%$. Even though large amounts of energy are converted into each other, the error of the total energy during the complete run is only $0.05\,\%$. Thus, energy is conserved with a very high accuracy and the not trivial coupling between hydrodynamics and gravity is resolved sufficiently. The internal energy of the system is given by the gas of the envelope only, as the DM particles do not posses internal energy. The expansion of the envelope due to the binary interaction causes the internal energy to decreases by $1.3 \times 10^{46}\,\mathrm{erg}$. This energy is released and further drives the expansion of the envelope.

Regarding angular momentum, large amounts are transferred from the DM particles to the envelope, as predicted by theory. The envelope gains $5.1 \times 10^{50}\,\mathrm{g\,cm^2/s}$ which accounts to an increase of $132\,\%$ until the end of the simulation time. Most of the angular momentum transfer takes place during the plunge-in ($111\,\%$ increase for the envelope). The error on the total angular momentum at the end of the simulations amounts to $4.2\,\%$, which demonstrates again that the resolution yields a high enough

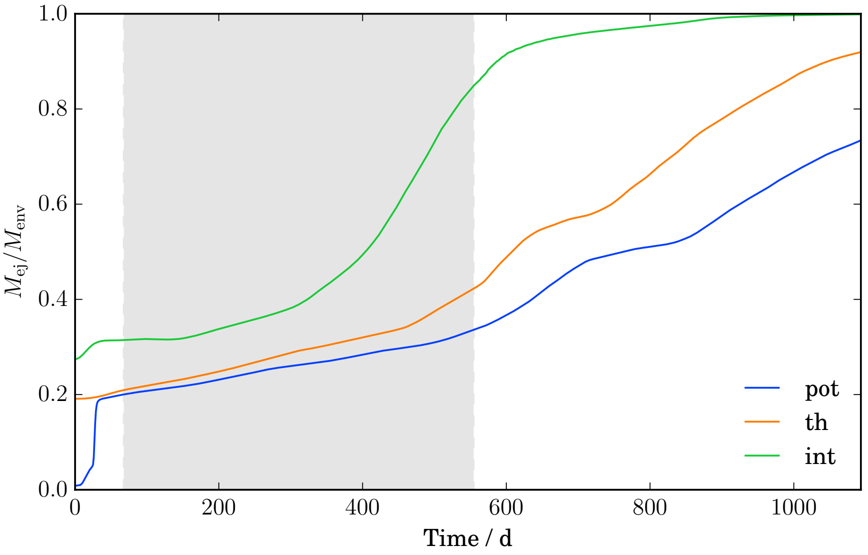

Figure 5.4: Evolution of unbound mass over the course of the simulation. Three different criteria to determine the unbound mass are displayed (pot: $e_{\mathrm{kin}} + e_{\mathrm{pot}} > 0$, th: $e_{\mathrm{kin}} + e_{\mathrm{pot}} + e_{\mathrm{th}} > 0$, int: $e_{\mathrm{kin}} + e_{\mathrm{pot}} + e_{\mathrm{int}} > 0$). The gray area marks the plunge-in phase.

accuracy.

The evolution of the fraction of unbound mass for different criteria is illustrated in Figure (5.4). We apply three different ways to determine which cells are unbound. The first one only takes into account the potential energy e_{pot} and the kinetic energy e_{kin}. Cells count as unbound if

$$e_{\mathrm{kin}} + e_{\mathrm{pot}} > 0 \tag{5.1}$$

is fulfilled. The second one also considers thermal energy e_{th} of the gas, hence the criterion reads

$$e_{\mathrm{kin}} + e_{\mathrm{pot}} + e_{\mathrm{th}} > 0. \tag{5.2}$$

As we use the OPAL equation of state, the complete internal energy of the gas is not only given by the thermal energy but also depends on the ionization energy. Therefore we can formulate a third criterion that regards the complete internal energy e_{int} of the gas:

$$e_{\mathrm{kin}} + e_{\mathrm{pot}} + e_{\mathrm{int}} > 0. \tag{5.3}$$

We will henceforth refer to these criteria as *potential*, *thermal*, and *internal* and to the fractions of unbound mass as f_{pot}, f_{th}, and f_{int} respectively.

As the placement of the companion in the computation domain at the start of the simulation enforces a recalculation of the energy contributions for the gas in the envelope, both the thermal and internal fractions of unbound mass are larger than zero at $t = 0\,\mathrm{d}$, namely $f_{\mathrm{th}} = 19\,\%$ and $f_{\mathrm{int}} = 27\,\%$. The *potential* criterion yields a initial value of $f_{\mathrm{pot}} = 0\,\%$, but also shows a rather erratic rise to $f_{\mathrm{pot}} = 18\,\%$ within the first 31 d of the simulation due to the initial set-up of the companion.

Regarding the *internal* criterion, we note a rapid rise of the fraction of unbound mass during the plunge-in, that is marked by the gray area in Figure (5.4). At the end of the plunge-in, a value of $f_{\mathrm{int}} = 84\,\%$ is reached and at the end of the simulation all but 0.1 % of the envelope mass is unbound. This would in principle indicate a complete ejection of the envelope under the assumption that the whole internal energy reservoir, including ionization energy, can be tapped and used to eject material. However, it is still under discussion, whether this assumption holds true. Ivanova (2018) states that convective flux is insufficient to remove the released recombination energy, which is therefore used as a work term and contributes to the envelope ejection. In contrast, Grichener et al. (2018) argue that most of the recombination energy is radiated away and claim that the contribution to the expansion and unbinding of the envelope is small.

The *thermal* criterion constitutes a more established approach by only taking into account the thermal energy of the gas. While f_{th} increases during the plunge-in to 42 %, most of the unbinding happens in the second half of the simulation. As we have seen before in Figure (5.1), the envelope expands and cools during this period. Consequently, recombination is triggered and contributes more strongly during the second half of the run to eject material. The released energy thermalizes and increases the thermal energy of the gas. At the end of the simulation, we still observe an increase in f_{th} and end up with a final value of $f_{\mathrm{th}} = 92\,\%$.

When analyzing the *potential* criterion, we notice a similar evolution as for the *thermal* one. There is only a small increase until the end of the plunge-in to $f_{\mathrm{pot}} = 33\,\%$. The final value amounts to 73 %, which still constitutes a significant ejection of mass. As recently shown in Ivanova (2018), the thermal energy of gas can most likely be used to drive the ejection mechanism, so that the *potential* criterion is likely to underestimate the expulsion of the gas. In the following chapters we will thus refer to unbound mass as defined by the *thermal* criterion, as it seems to deliver the most compelling and relevant values.

In Figure (5.5), the ionization energy is plotted for different times during the simulation. The ionization state of the gas is calculated by solving the Saha equations in the local thermodynamic equilibrium for H and He, which yields the ionization energy, the fraction of electrons and the different ionization states of the H and He. As more massive elements are ignored, the electron fraction is expected to be underestimated. However, this still allows us to evaluate the spatial positioning of neutral and ionized elements. In the first panel of Figure (5.5), the long tidal arm formed by the trajectory of the companion through the envelope is clearly shown as a region of high ionization energy. This is due to the high temperature and pressure close to the shock front. However, in the area behind the shock front, the gas expands and cools, thus triggering recombination and the releasing the corresponding ionization

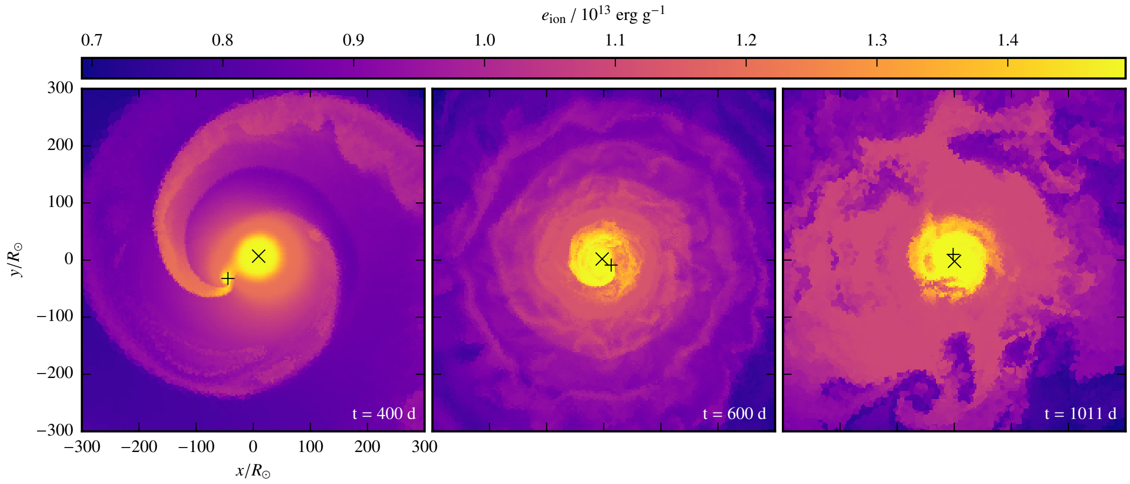

Figure 5.5: Time series of the specific ionization energy. The positions of the RG core and the companion are marked by × and + respectively.

energy. The released energy can be converted into mechanical energy and thereby contributes to eject the envelope.

5.3 Conclusion

The CE simulation presented in this chapter explores a first set-up that is suitable to emulate the formation process of a sdB star in a close binary with a low-mass stellar companion of $M_{\rm comp} = 0.1\,{\rm M}_\odot$. We show that the AREPO code can produce results that have very high accuracy for both energy and angular momentum conservation. We are able to follow the complete plunge-in phase and the subsequent evolution for further 530 days.

The most important quantity for this run is the ejected mass. As pointed out in the Section (1.2), CEE is likely to be a primary formation channel for many of the observed close sdB binary systems. We reach a fraction of unbound mass of 92 %, which demonstrates that even small companion masses can trigger significant and almost complete envelope ejections.

6 The Influence of Initial Parameters

In this chapter, we explore CE simulations set up in the same way as described in Section (5), but with varying initial parameters. We first conduct a resolution study to analyze the influence of the refinement criterion around the DM particles on the simulation outcome. Subsequently, we try to deduce the influence of the companion's mass on the properties of the final system. Special interest is given the dependence of the ejected mass on the mass ration between progenitor and companion.

6.1 Resolution Study

Using the same set-up as described in Section (5.1), we conduct a resolution study with a $0.77\,\mathrm{M}_\odot$ RG and a companion of a mass of $0.1\,\mathrm{M}_\odot$. In order to evaluate the influence of the refinement criterion around the point masses, we conduct four simulations with identical starting parameters except for the imposed cells per softening length around the two point masses. We chose 10, 20, 30 and 40 cells per softening length. A summary of the outcome of these simulations is given in Table (6.1).

n_c	$d_\mathrm{f}/R_\odot$	P_f/d	e_f	$\Delta E/E_0$	$\Delta L/L_0$	$N/10^6$
10	107.8	171.8	0.17	0.3%	0.14%	2.51
20	34.3	30.1	0.19	0.2%	3.8%	2.68
30	12.1	6.5	0.021	0.06%	3.4%	3.01
40	12.3	6.6	0.016	0.05%	4.2%	3.26

Table 6.1: Overview of the results of the resolution runs. Given are the the upper limit of the number of cells per softening length n_c, the final separation between the point masses d_f, the final period P_f, the energy error with $\Delta E = |E_0 - E_\mathrm{f}|$ (E_0: initial value of the total energy, E_f: final value of the total energy), the ejected mass M_ej and the number of cells N. All final values refer to $t = 1080\,\mathrm{d}$.

Unsurprisingly, the numbers show that the higher the resolution around the point masses the lower the energy of the total error becomes. Generally, it is remarkable how well the total energy is conserved for all of the resolution runs. Comparing the highest resolution run with 40 cells per softening length to the lowest one with 10, the energy conservation improves from $0.3\,\%$ to $0.05\,\%$, which is more accurate by a factor of five. Since we impose more cells per softening length at the higher resolution runs, the number of total cells in the computation domain increases by a factor of around 1.3 from 2.51×10^6 to 3.26×10^6. Without the additional refinement

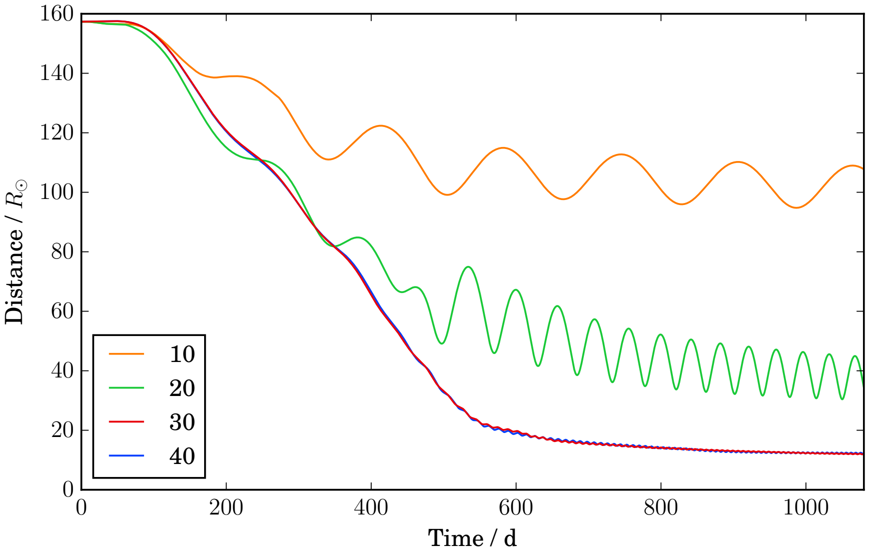

Figure 6.1: Dependence of the distance evolution on resolutions around point masses. Four simulations for 10, 20, 30 and 40 cells per softening length around the point masses are displayed.

criterion around the cores, we would be left with only 10^6 cells, since this was set as the target number of cells for refinement by mass only. Hence, the additional refinement around the DM particles lead to a considerable increase of cells.

Even though the energy errors for the low resolution runs seem to be acceptably small, checking the other results makes it quite clear that there are not sufficient cells around the companion. In consequence, less energy can be extracted from the two point masses. So the final distance between the companion and core of the RG still amounts to $107.8\,\mathrm{R}_\odot$ for the lowest resolution, in contrast to the highest resolution, that stopped at a separation of $12.3\,\mathrm{R}_\odot$. Due to the same reason, the orbit of the higher resolution run is less elliptical. Moreover, the difference in the final period, which still accounts to 171.8 d at low resolution shrinks to only 6.6 d at high resolution.

In Figure (6.1), the separation between the two point masses for the different resolutions is illustrated. For both 10 and 20 cells per softening length, the higher eccentricity and impeded spiral-in is clearly recognizable. However, 30 and 40 cells per softening length display an agreement of the development of the separation both during the plunge-in and for the stabilized orbit afterwards. We conclude that the resolution of both 30 and 40 cells is sufficient to resolve the conversion of different types of energy with a high enough accuracy. To be on the safe side, we chose 40 cells per softening length for all of the subsequent simulation runs.

6.2 The Effect of Varying Companion Masses

M_{comp}	$t_{\mathrm{f}}/\mathrm{d}$	$d_{\mathrm{i}}/R_{\odot}$	$d_{\mathrm{f}}/R_{\odot}$	$P_{\mathrm{f}}/\mathrm{d}$	e_{f}	$\Delta E/E_0$	$\Delta L/L_0$	$M_{\mathrm{ej}}/M_{\mathrm{env}}$	$N/10^6$
0.01	1500	123.7	23.0	18.5	0.041	0.06%	0.57%	25.2%	3.01
0.03	1000	135.5	5.6	2.2	0.050	0.06%	5.02%	34.0%	2.96
0.04	1023	139.8	6.8	2.9	0.034	0.08%	0.81%	55.1%	3.18
0.05	917	143.4	7.9	3.5	0.030	0.07%	3.55%	62.1%	3.20
0.063	847	147.8	8.4	3.9	0.055	0.04%	4.08%	70.8%	3.21
0.1	1094	157.3	12.3	6.6	0.016	0.05%	4.23%	92.0%	3.26

Table 6.2: Overview of the simulation runs with different companion masses. Given is the the companion mass M_{comp} in solar units, the final time of the simulation t_{f}, the initial and final separation between the point masses $d_{\mathrm{i,f}}$, the final period P_{f}, the final eccentricity e_{f}, the energy error with $\Delta E = |E_0 - E_{\mathrm{f}}|$ (E_0: initial value of the total energy, E_{f}: final value of the total energy), the angular momentum error $\Delta L = |L_0 - L_{\mathrm{f}}|$ (L_0: initial value of the total angular momentum, L_{f}: final value of the total angular momentum), the fraction of ejected mass $M_{\mathrm{ej}}/M_{\mathrm{env}}$ and the final number of cells N. All simulations started with $N_{\mathrm{i}} = 2.44 \times 10^6$ cells and at 80 % RLOF distance.

In this section, we will analyze the influence of the companion mass on the final properties of the binary system. A special focus lies on the question if a lower threshold for the companion mass can be found, so that lowering the mass even further will not lead to any significant disruption of the RG primary and mass ejection is prevented. This is interesting, as observations show that sdB stars in close binaries with very low mass companions exist (Section 1.3).
We conduct several runs that follow the set-up procedure used for the simulation described in detail in Chapter (5). Hence, all of the simulations use the same RG progenitor star with a core mass of $M_{\mathrm{c}} = 0.47\,\mathrm{M}_{\odot}$ and an envelope mass of $M_{\mathrm{env}} = 0.30\,\mathrm{M}_{\odot}$. The initial resolution of the runs is approximately 2.44×10^6 and we impose 40 cells per softening length around the DM particles, as in the previous chapter. However, instead of using a mass of $0.1\,\mathrm{M}_{\odot}$ for the companion, we chose even lower masses that all lie in the sub-stellar regime, namely $0.01\,\mathrm{M}_{\odot}$, $0.03\,\mathrm{M}_{\odot}$, $0.04\,\mathrm{M}_{\odot}$, $0.05\,\mathrm{M}_{\odot}$ and $0.063\,\mathrm{M}_{\odot}$. The initial distance was always set relative to the RLOF distance at 80 %, which makes it different for each model. Nonetheless, this should make the different runs more comparable than just placing each companion at the same distance, since the distance to the RLOF is more representative of the stage of the CEE the system is in.

In Figure (6.2), the evolution of the binary separation for different companion masses is plotted until $t = 1250\,\mathrm{d}$. All of the systems start with a separation between $120\,\mathrm{R}_{\odot}$ and $160\,\mathrm{R}_{\odot}$, in descending initial distance with decreasing companion mass, due to the shift in the RLOF distance. The evolution of the highest companion mass of $M_{\mathrm{comp}} = 0.1\,\mathrm{M}_{\odot}$ shows the most rapid plunge-in and the subsequent stabilization

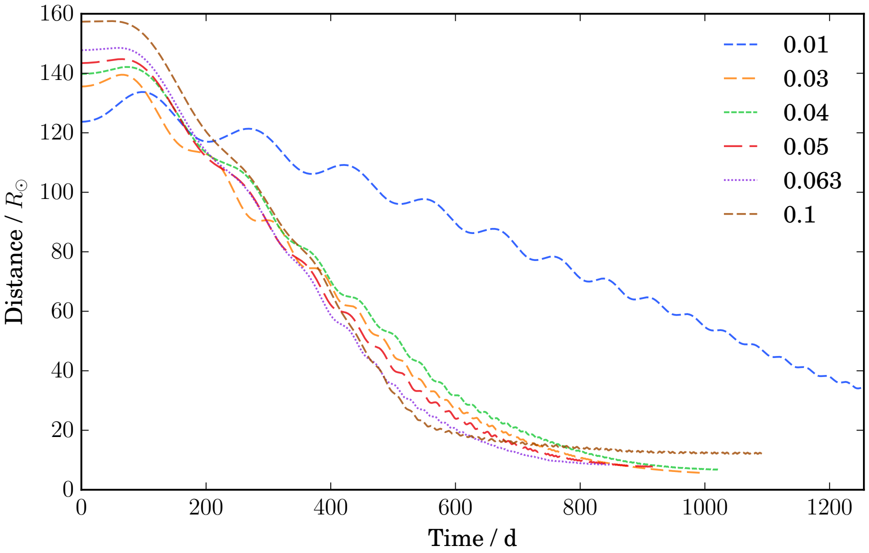

Figure 6.2: Evolution of the binary separation for different companion masses. The legend indicates the respective mass of the companion in solar masses.

of the orbit sets in the fastest. In Table (6.2), an overview of the most important results of the comparison runs is listed with the exact numbers for the initial an final distances. There is a clear trend for closer final separations with decreasing mass, while the plunge-in phase takes longer. This can be explained by the fact that for smaller masses, less energy is extracted by a shrinking of the orbit. Hence, it takes longer to eject most of the mass enclosed by the orbit, which is the important condition for a stop of the plunge-in. In consequence, we chose longer simulation times for lower companion masses in an effort to capture the end of the plunge-in and several subsequent orbits. Comparing with Figure (6.2), we succeed to do so for all companion masses but the smallest one of $M_{\mathrm{comp}} = 0.01\,\mathrm{M}_\odot$, which is, even at $t = 1500\,\mathrm{d}$, still spiralling inwards. This makes the final results hard to compare to the other runs. We end with a separation of $d_{\mathrm{f}} = 23\,\mathrm{R}_\odot$ and a period of $P_{\mathrm{f}} = 18.5\,\mathrm{d}$. Taking out the lowest mass, we observe a trend to less eccentricity with higher companion mass. All of the runs show very accurate conservation of energy with energy errors below 0.1 %. The error for the angular momentum stays below 6 % for all of the different companion masses. The final number of cells in the computational domain increases with the mass of the companion, which is to be expected, as more cells will be created around the point particle of the companion, if its mass is higher. The most interesting result of these runs consists in the percentage of ejected mass. We apply the *thermal* criterion to determine the fraction of unbound mass, as described in detail in Section (5.2). It is clear that for higher companion masses more dynamic interaction takes place and we expect higher percentages of expelled gas. This is reflected by the results listed. We notice an almost complete ejection for the run with the highest companion mass, while for the lowest mass we observe

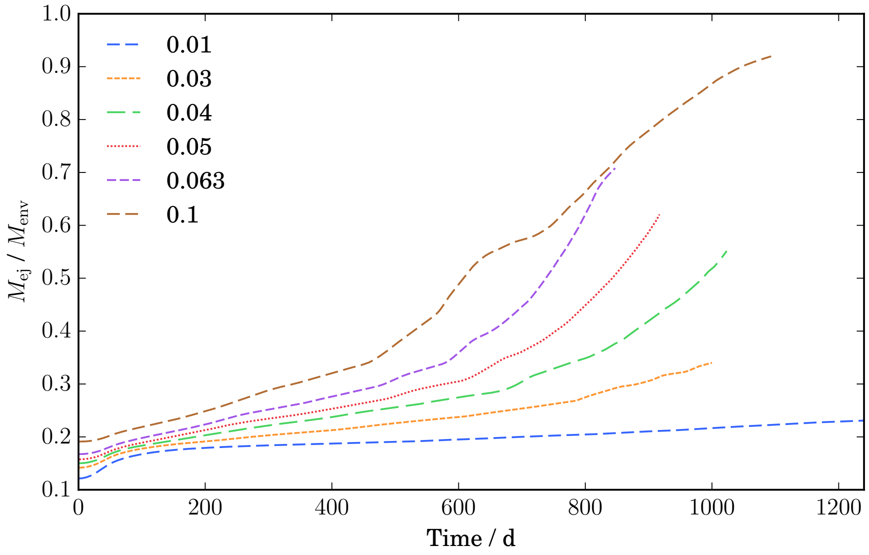

Figure 6.3: Evolution of the ejected mass for different companion masses. The legend indicates the respective mass of the companion in solar masses. The following condition on the energy of the cell determines whether it counts as unbound: $e_{\mathrm{kin}} + e_{\mathrm{pot}} + e_{\mathrm{th}} > 0$.

almost no ejection after the initial jump caused by the numerical recalculation of the energy contributions. In Figure (6.3) the evolution of the unbound mass under the *thermal* criterion is displayed for the comparison runs. We note that for the three middle sized companions the fraction of unbound mass is still increasing steeply at the end of the simulation, even though we saw before that the plunge-in phase has already come to a halt. This is caused by the release of recombination energy, that is delayed until gas cools down sufficiently. Unfortunately, longer simulation of these systems to track the unbinding of mass after that point is very costly, since the two point particles are very close.

To compare the final structure of the simulations, density slices through the x-and y-plane of the grid are displayed centered on the center of mass in Figure (6.4). The density ranges from $1 \times 10^{-9}\,\mathrm{g\,cm^{-3}}$ to $1 \times 10^{-5}\,\mathrm{g\,cm^{-3}}$ for all of the plots. The mass of the companion in solar masses is stated in the lower left and the final time of the simulation in the lower right corner of each panel. Once again, it is shown clearly that the envelope is almost completely ejected for the run with $M_{\mathrm{comp}} = 0.1\,\mathrm{M}_{\odot}$. The runs for $M_{\mathrm{comp}} = 0.04\,\mathrm{M}_{\odot}$, $M_{\mathrm{comp}} = 0.05\,\mathrm{M}_{\odot}$ and $M_{\mathrm{comp}} = 0.063\,\mathrm{M}_{\odot}$ all exhibit a turbulent envelope structure. There is more mass left, but due to the effects of recombination, more gas might become unbound if the simulation could be run for longer times. For the remaining two simulations with even lower companion masses, we observe a layered structure around the point particles. When comparing the large-scale shape of the RG envelope, especially in the outer parts, we note much less disruption. The tidal arms and shock fronts caused by these low mass

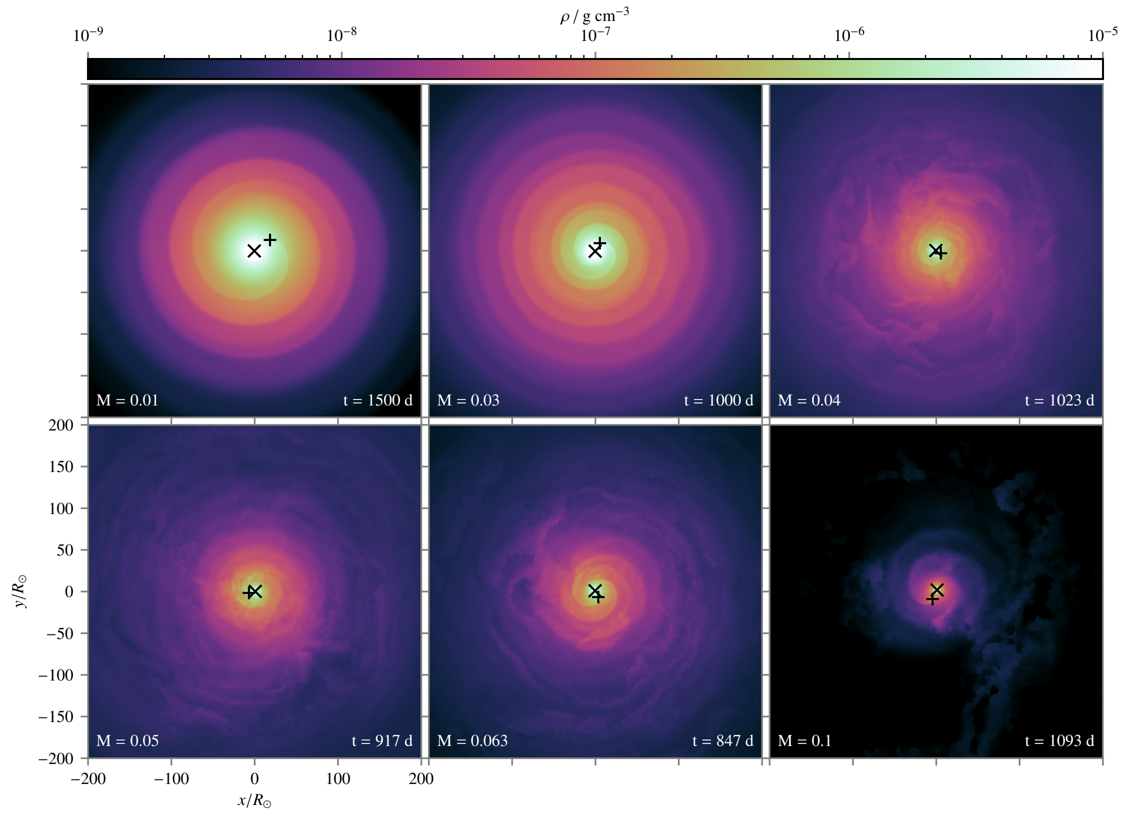

Figure 6.4: Final density slice in the x-y plane for different companion masses. The mass of the companion in solar masses is given in the lower left and the final time on the lower right corner of each panel. The positions of the cores of the RG primary and the companion are marked by an × and + respectively. Each frame is centered on the center of mass of the binary system.

companions are less extended and do not necessarily lead to an initial unbinding of mass during the plunge-in.

6.3 Discussion

In this chapter, we first conducted a resolution study to determine the necessary resolution around the DM particles to capture the physics of the CEE with light companions. We concluded that 40 cells per softening length around the cores suffice to resolve the hydrodynamic interactions.

Subsequently, we examined the influence of the companion's mass on the outcome of the system after the plunge-in phase. We observe a qualitatively similar behavior of the distance evolution for all but the lowest mass. This might indicate that $M_{\text{comp}} = 0.01\,\mathrm{M}_\odot$ represents a lower mass threshold for triggering significant dynamic interaction. However, when comparing the evolution of the separation (Figure 6.2), we also see that the lowest mass companion does not show the same general shape of the slope as all the other runs. The plunge-in phase is not really discernable for the lightest companion. This could also suggest that the resolution for this specific run is not high enough anymore to model the gravitational interaction. In consequence, another resolution study should be conducted to make a more conclusive statement about the lower threshold of the companion mass. Due to the limitations in computing time, this is, unfortunately, not feasible for this work. Nevertheless, we were able to show that even companions as light as $0.04\,\mathrm{M}_\odot$ lead to a fraction of unbound mass of 55 % with a strong tendency to grow larger. This shows that even BD-like compact companions can play important roles in the evolution of CE systems and indicates that the recent observations of sdB binary systems with light companions are indeed the result of a previous CEE.

7 Conclusion

The CE phase is an essential step in the formation of close binaries, as it allows the angular momentum to be transferred from the compact objects of the binary to the gas of the envelope and constitutes an important sink for energy. CEE is connected to a large range of astrophysical phenomena, including type Ia supernovae, cataclysmic variables, WD binaries and mergers. While there has been recent progress, many of the underlying physical processes of the CEE are still poorly understood. In this work, we use the state of the art code AREPO, that brings the benefit of both grid-based and Lagrangian approaches together, to model the CE phase of sdB stars.
The first chapter summarized the properties of sdB stars, explained the formation process through CEE and gave a short overview of the current observational state. Afterwards, an overview addressing CE physics is presented, followed by a short delineation of the numerical methods used. Subsequently, the generation of an initial stable model that resembles a progenitor sdB star is explained. Having presented the results of a first CE simulation with a light companion in the next chapter, we conclude with a parameter study on the resolution and initial mass of the companion.

7.1 Achievements

Recent observations have demonstrated the existence of sdB stars in binary systems with low mass companions (Schaffenroth et al., 2014, 2015, 2017). Considering that the formation of sdB stars requires the unbinding of the progenitor RG star's envelope, this work addresses the question whether low mass companions are sufficient to trigger envelope ejection.
The main results of this work can be summarized in the following points:

1. Using the mapping process developed by **?** allows us to use a stellar profile generated by the MESA code as an initial model in AREPO. The subsequent relaxation following **?**, results in a stable three-dimensional model that is a good representation of a star at the tip of the RGB and hence a suitable progenitor for an sdB star.

2. We can apply and adapt the AREPO code to conduct hydrodynamic simulations for the CEE of sdB progenitors with very high accuracy. The additional refinement criteria around the DM particles result in a resolution suitable to emulate the underlying physical processes and simulate the different phases of the CEE.

3. We have seen that even for very low masses of the companion, an almost complete unbinding of the envelope can take place. A final value of $M_{\mathrm{ej}}/M_{\mathrm{env}} =$

92 % is reached for a companion mass of $M_{\text{comp}} = 0.1\,\mathrm{M}_{\odot}$. Lowering the companion mass even further to $M_{\text{comp}} = 0.05\,\mathrm{M}_{\odot}$ still leads considerable envelope ejection of $M_{\text{ej}}/M_{\text{env}} = 62\,\%$. Regarding the evolution of the fraction of unbound mass, there is good reason to assume that further ejection would take place for a longer simulation times. Consequently, even companion masses in the BD regime appear to be sufficient to cause almost complete envelope ejection. This is further evidence for the importance of CEE for the formation of sdB binaries and agrees with recent observations.

7.2 Outlook

In the course of this work, we have come across some points that could be addressed to improve and confirm our results. First, future simulations could make an effort to capture even more physical phenomena, like magnetic fields. While **?** demonstrates that the dynamical impact is small, it would still yield a measure that could be compared to observations. Furthermore, a scheme to model accretion onto the companion could be implemented. Even though Chamandy et al. argues that accretion rates are significantly below the Bondi-Hoyle-Lyttleton rate and hence do not have a big impact on the outcome, it might still be interesting to see how the mass of the companion evolves.

One parameter that could not be investigated in this work due to the limited time is the influence of the mass of the sdB progenitor. As all stars with initial masses from $0.8\,\mathrm{M}_{\odot}$ to $2\,\mathrm{M}_{\odot}$ posses almost identical cores at the tip of the RGB, there is a degeneracy for the sdB progenitor. It would thus be interesting to see how the initial mass influences the resulting sdB binary system.

Nomenclature

GH Gemeinsame Hülle

BD brown dwarf

ZAMS zero age main sequence

CEE common envelope evolution

EOS equation of state

DM dark matter

AMR adaptive mesh refinement

SPH smoothed particle hydrodynamics

RGB red giant branch

RLOF Roche lobe overflow

RL Roche lobe

sdB hot subluminous B-type

SdB hot subluminous B-type

CE common envelope

EHB extreme horizontal branch

HB horizontal branch

HR Hertzsprung-Russell

RG red giant

MS main sequence

RGB red giant branch

NS neutron star

BH black hole

WD white dwarf

Part I

Appendix

A Lists

1.1 List of Figures

1.1 **Formation channel for sdB stars through CEE with an MS companion.** The core of the evolved RG is depicted in purple and the surrounding mass of the envelope in red. After the CE phase, the core of the RG remains as a sdB star in a close binary with the companion. The figure is modified from Podsiadlowski et al. (2008). . . 2

1.2 **Diagram of the companion mass over period for known HR Vir systems.** The hydrogen burning limit is indicated by the gray horizontal bar. All companions below are in the sub-stellar regime. The red line depicts the minimal possible period for a specific mass and is based on the assumption that the companions cannot exceed the Roche limit. The figure is take from Schaffenroth et al. (2017). . . 3

4.1 **Evolutionary track of a one solar-mass star simulated by MESA.** Different stages are annotated as ZAMS: Zero age main sequence, SGB: Subgiant branch, RGB: Red giant branch, RGT: Tip of the red giant branch and HR: Horizontal branch. We use the profile right at the tip of the RGB as our progenitor for the AREPO runs. . . 15

4.2 **Hydrostatic equilibrium for the relaxation run at different times.** In the top panel, both pressure gradient (dashed line) and gravitational potential (solid line) are plotted. The lower panel depicts the deviation from the hydrostatic equilibrium. The blue line for $t = 0\,\mathrm{d}$ is derived from the initial MESA profile, as described in Section (4.2). 19

4.3 **Mach number and density profile for the relaxation run at different times.** The upper panel shows the Mach number over the radius. The lower panel illustrates the density profile of the star. . . . 20

5.1 **Time series of density snapshots in the x-y plane at six different times.** The positions of the cores of the RG primary and the companion are marked by an × and + respectively. Each frame is centered on the center of mass of the binary system. The inset in the last panel zooms in on the central square region with an edge length of $20\,\mathrm{R}_\odot$ with a color scale comprising values from 10^{-5} to 10^{-8} $\mathrm{g\,cm^{-3}}$. 23

5.2 **Evolution of the separation between point particles and orbital trajectories.** The main panel displays the distance between the two point particles during the simulation time. The inset shows the position of companion's core in blue and the position of the core of the RG in red. 24
5.3 **Overview of the potential and kinetic energy of the DM particles and the gas particles of the envelope.** The gray area indicates the plunge-in phase. 24
5.4 **Evolution of unbound mass over the course of the simulation.** Three different criteria to determine the unbound mass are displayed (pot: $e_{\mathrm{kin}}+e_{\mathrm{pot}} > 0$, th: $e_{\mathrm{kin}}+e_{\mathrm{pot}}+e_{\mathrm{th}} > 0$, int: $e_{\mathrm{kin}}+e_{\mathrm{pot}}+e_{\mathrm{int}} > 0$). The gray area marks the plunge-in phase. 26
5.5 **Time series of the specific ionization energy.** The positions of the RG core and the companion are marked by × and + respectively. 28

6.1 **Dependence of the distance evolution on resolutions around point masses.** Four simulations for 10, 20, 30 and 40 cells per softening length around the point masses are displayed. 30
6.2 **Evolution of the binary separation for different companion masses.** The legend indicates the respective mass of the companion in solar masses. 32
6.3 **Evolution of the ejected mass for different companion masses.** The legend indicates the respective mass of the companion in solar masses. The following condition on the energy of the cell determines whether it counts as unbound: $e_{\mathrm{kin}} + e_{\mathrm{pot}} + e_{\mathrm{th}} > 0$. 33
6.4 **Final density slice in the x-y plane for different companion masses.** The mass of the companion in solar masses is given in the lower left and the final time on the lower right corner of each panel. The positions of the cores of the RG primary and the companion are marked by an × and + respectively. Each frame is centered on the center of mass of the binary system. 34

1.2 List of Tables

6.1 **Overview of the results of the resolution runs.** Given are the the upper limit of the number of cells per softening length n_{c}, the final separation between the point masses d_{f}, the final period P_{f}, the energy error with $\Delta E = |E_0 - E_{\mathrm{f}}|$ (E_0: initial value of the total energy, E_{f}: final value of the total energy), the ejected mass M_{ej} and the number of cells N. All final values refer to $t = 1080\,\mathrm{d}$. 29

6.2 **Overview of the simulation runs with different companion masses.** Given is the the companion mass M_{comp} in solar units, the final time of the simulation t_{f}, the initial and final separation between the point masses $d_{\mathrm{i,f}}$, the final period P_{f}, the final eccentricity e_{f}, the energy error with $\Delta E = |E_0 - E_{\mathrm{f}}|$ (E_0: initial value of the total energy, E_{f}: final value of the total energy), the angular momentum error $\Delta L = |L_0 - L_{\mathrm{f}}|$ (L_0: initial value of the total angular momentum, L_{f}: final value of the total angular momentum), the fraction of ejected mass $M_{\mathrm{ej}}/M_{\mathrm{env}}$ and the final number of cells N. All simulations started with $N_{\mathrm{i}} = 2.44 \times 10^6$ cells and at 80 % RLOF distance. . 31

B Bibliography

L. Chamandy, Y. Tu, E. G. Blackman, J. Carroll-Nellenback, A. Frank, B. Liu, and J. Nordhaus. Energy budget and core-envelope motion in common envelope evolution. *Monthly Notices of the Royal Astronomical Society*, 486(1):1070–1085, 2019. ISSN 0035-8711. doi: 10.1093/mnras/stz887.

J. D. M. Dewi and T. M. Tauris. On the Energy Equation and Efficiency Parameter of the Common Envelope Evolution. *Astronomy and Astrophysics, Vol. 360, p.1043-1051*, 360:1043–1051, jul 2000. ISSN 0004-6361. URL `http://arxiv.org/abs/astro-ph/0007034`.

S. Geier, V. Schaffenroth, H. Drechsel, U. Heber, T. Kupfer, A. Tillich, R. H. Østensen, K. Smolders, P. Degroote, P. F. L. Maxted, B. N. Barlow, B. T. Gänsicke, T. R. Marsh, and R. Napiwotzki. BINARIES DISCOVERED BY THE MUCHFUSS PROJECT: SDSS J08205+0008-AN ECLIPSING SUBDWARF B BINARY WITH A BROWN DWARF COMPANION. *The Astrophysical Journal Letters*, 731(5pp):22, 2011. doi: 10.1088/2041-8205/731/2/L22. URL `https://iopscience.iop.org/article/10.1088/2041-8205/731/2/L22/pdf`.

L. Girardi. Red Clump Stars. *Annual Review of Astronomy and Astrophysics*, 54(1):95–133, sep 2016. ISSN 0066-4146. doi: 10.1146/annurev-astro-081915-023354. URL `http://www.annualreviews.org/doi/10.1146/annurev-astro-081915-023354`.

A. Grichener, E. Sabach, and N. Soker. The limited role of recombination energy in common envelope removal. *Monthly Notices of the Royal Astronomical Society*, 478(2):1818–1824, mar 2018. ISSN 13652966. doi: 10.1093/mnras/sty1178. URL `http://arxiv.org/abs/1803.05864http://dx.doi.org/10.1093/mnras/sty1178`.

Z. Han, P. Podsiadlowski, and P. P. Eggleton. The formation of bipolar planetary nebulae and close white dwarf binaries. Technical report, 1995.

U. Heber. Hot Subdwarf Stars. *Annual Review of Astronomy and Astrophysics*, 47(1):211–251, sep 2009. ISSN 0066-4146. doi: 10.1146/annurev-astro-082708-101836. URL `www.annualreviews.orghttp://www.annualreviews.org/doi/10.1146/annurev-astro-082708-101836`.

U. Heber. Hot subluminous stars. *Publications of the Astronomical Society of the Pacific*, 128(966), 2016. ISSN 00046280. doi: 10.1088/1538-3873/128/966/082001. URL `https://arxiv.org/pdf/1604.07749.pdf`.

N. Ivanova. On the Use of Hydrogen Recombination Energy during Common Envelope Events. *The Astrophysical Journal*, 858(2):L24, may 2018. ISSN 2041-8213. doi: 10.3847/2041-8213/aac101. URL http://stacks.iop.org/2041-8205/858/i=2/a=L24?key=crossref.e4f18cc8ab78b9d83937723a060a03f3.

N. Ivanova and J. L. Nandez. Common envelope events with low-mass giants: Understanding the transition to the slow spiral-in. *Monthly Notices of the Royal Astronomical Society*, 462(1):362–381, jun 2016. ISSN 13652966. doi: 10.1093/mnras/stw1676. URL http://arxiv.org/abs/1606.04923http://dx.doi.org/10.1093/mnras/stw1676.

N. Ivanova, S. Justham, X. Chen, O. De Marco, C. L. Fryer, E. Gaburov, H. Ge, E. Glebbeek, Z. Han, X. D. Li, G. Lu, T. Marsh, P. Podsiadlowski, A. Potter, N. Soker, R. Taam, T. M. Tauris, E. P. Van Den Heuvel, and R. F. Webbink. Common envelope evolution: Where we stand and how we can move forward, 2013. ISSN 09354956. URL https://arxiv.org/pdf/1209.4302.pdf.

Kippenhahn. *Stellar structure & evolution*. 2012. ISBN 9783642302558. doi: 10.1007/978-3-642-61523-8.

P. F. Maxted, U. Heber, T. R. Marsh, and R. C. North. The binary fraction of extreme horizontal branch stars. *Monthly Notices of the Royal Astronomical Society*, 326(4):1391–1402, 2001. ISSN 00358711. doi: 10.1111/j.1365-2966.2001.04714.x. URL https://academic.oup.com/mnras/article-abstract/326/4/1391/1065734.

J. L. A. Nandez, N. Ivanova, and J. C. Lombardi. Recombination energy in double white dwarf formation. *MNRAS*, 450:39–43, 2015. doi: 10.1093/mnrasl/slv043. URL https://academic.oup.com/mnrasl/article-abstract/450/1/L39/985979.

G. Nelemans. Reconstructing the evolution of double helium white dwarfs: Envelope loss without spiral-in. *Astronomy and Astrophysics*, 360(3):1011–1018, jun 2000. ISSN 00046361. URL http://arxiv.org/abs/astro-ph/0006216.

S. T. Ohlmann, F. K. Röpke, R. Pakmor, V. Springel, and E. Müller. Magnetic field amplification during the common envelope phase. *Monthly Notices of the Royal Astronomical Society: Letters*, 462(1):L121–L125, jul 2016. ISSN 17453933. doi: 10.1093/mnrasl/slw144. URL http://mnrasl.oxfordjournals.org/http://arxiv.org/abs/1607.05996http://dx.doi.org/10.1093/mnrasl/slw144.

B. Paxton, M. Cantiello, P. Arras, L. Bildsten, E. F. Brown, A. Dotter, C. Mankovich, M. H. Montgomery, D. Stello, F. X. Timmes, and R. Townsend. Modules for experiments in stellar astrophysics (MESA): Planets, oscillations, rotation, and massive stars. *Astrophysical Journal, Supplement Series*, 208(1):4, aug 2013. ISSN 00670049. doi: 10.1088/0067-0049/208/

1/4. URL http://stacks.iop.org/0067-0049/208/i=1/a=4?key=crossref.9ac89c257bf3021e94c56104e0913fc9.

B. Paxton, P. Marchant, J. Schwab, E. B. Bauer, L. Bildsten, M. Cantiello, L. Dessart, R. Farmer, H. Hu, N. Langer, R. H. Townsend, D. M. Townsley, and F. X. Timmes. Modules for Experiments in Stellar Astrophysics (MESA): Binaries, pulsations, and explosions. *Astrophysical Journal, Supplement Series*, 220(1):15, sep 2015. ISSN 00670049. doi: 10.1088/0067-0049/220/1/15. URL http://stacks.iop.org/0067-0049/220/i=1/a=15?key=crossref.26e842ea2ce21ffeccd7e7c05ee152d2.

P. Podsiadlowski, Z. Han, A. E. Lynas-Gray, and D. Brown. Hot Subdwarfs in Binaries as the Source of the Far-UV Excess in Elliptical Galaxies. *ASP Conference Series*, 392:15—-, aug 2008. URL http://arxiv.org/abs/0808.0574http://arxiv.org/abs/0808.0574{%}5Cnpapers3://publication/uuid/C971279B-7C3B-464D-8179-090D0FA62956{%}5Cnpapers3://publication/uuid/F7096D11-C48E-4FCA-B2D1-189EAA267B44.

F. J. Rogers and A. Nayfonov. UPDATED AND EXPANDED OPAL EQUATION-OF-STATE TABLES: IMPLICATIONS FOR HELIOSEISMOLOGY. Technical report. URL https://iopscience.iop.org/article/10.1086/341894/pdf.

V. Schaffenroth, L. Classen, K. Nagel, S. Geier, C. Koen, U. Heber, and H. Edelmann. Astrophysics Two candidate brown dwarf companions around core helium-burning stars. *Astronomy and Astrophysics*, 570:70, 2014. doi: 10.1051/0004-6361/201424616. URL http://www.aanda.org.

V. Schaffenroth, B. N. Barlow, H. Drechsel, and B. H. Dunlap. An eclipsing post common-envelope system consisting of a pulsating hot subdwarf B star and a brown dwarf companion. *Astronomy and Astrophysics*, 576:123, 2015. ISSN 14320746. doi: 10.1051/0004-6361/201525701. URL https://www.aanda.org/articles/aa/pdf/2015/04/aa25701-15.pdf.

V. Schaffenroth, B. Barlow, S. Geier, M. Vučković, D. Kilkenny, and J. Schaffenroth. News from the erebos project. *Open Astronomy*, 26(1):208–213, dec 2017. ISSN 25436376. doi: 10.1515/astro-2017-0438. URL http://www.degruyter.com/view/j/astro.2017.26.issue-1/astro-2017-0438/astro-2017-0438.xml.

V. Springel. The cosmological simulation code GADGET-2, may 2005. ISSN 00358711. URL http://arxiv.org/abs/astro-ph/0505010http://dx.doi.org/10.1111/j.1365-2966.2005.09655.x.

V. Springel. E pur si muove: Galilean-invariant cosmological hydrodynamical simulations on a moving mesh. *Monthly Notices of the Royal Astronomical Society*, 401(2):791–851, jan 2010. ISSN 00358711. doi: 10.1111/j.1365-2966.2009.15715.x. URL https://academic.oup.com/mnras/article-lookup/doi/10.1111/j.1365-2966.2009.15715.x.

Erklärung:

Ich versichere, dass ich diese Arbeit selbstständig verfasst habe und keine anderen als die angegebenen Quellen und Hilfsmittel benutzt habe.

Heidelberg, den (Datum) ....